CrossMark

High Precision SEIS Calibration for the InSight Mission and Its Applications

L. Pou[1] · D. Mimoun[1] · P. Lognonne[2] · R.F. Garcia[1] ·
O. Karatekin[3] · M. Nonon-Latapie[4] · R. Llorca-Cejudo[4]

Abstract Part of the InSight mission, the SEIS instrument (Seismic Experiment for Interior Structures), is planned to arrive on Mars in November 2018. In order to prepare its future recordings on the red planet, special attention was directed towards calibrating the seismometer in-situ on the Martian surface. Besides relative calibrations, we studied the possibility of actively calibrating the two kinds of seismometers onboard SEIS, the Very Broad Band seismometers (VBB) and the Short Period seismometers (SP) and extended the analysis towards a possible absolute calibration. For that purpose, we developed additional noise models at low frequency and elaborate on how they will be sensed by the seismic sensors from long-period data recorded by the seismometer. Such work will improve SEIS

✉ L. Pou
l.pou@isae.fr

D. Mimoun
mimoun@isae.fr

P. Lognonne
lognonne@ipgp.fr

R.F. Garcia
raphael.garcia@isae-supaero.fr

O. Karatekin
ozgur.karatekin@observatory.be

M. Nonon-Latapie
michel.nonon@cnes.fr

R. Llorca-Cejudo
roger-llorca-cejudo@cnes.fr

[1]   DEOS/SSPA, ISAE-Supaero, Toulouse, France

[2]   IPGP, Paris, France

[3]   Royal Observatory of Belgium, Brussels, Belgium

[4]   CNES, Toulouse, France

capabilities to unveil the inner structure of Mars by checking SEIS well-being and with applications such as gravimetry with the main Phobos tide. The current calibration procedure is planned to take one hour to calibrate the VBB sensors using the SP sensors, and determine the VBB gain with an accuracy of 0.4%, good enough to resolve the state of the Martian core.

1 Introduction

SEIS (Fig. 1) is a hybrid three-axis seismometers, compromised of a 3-axis very broad band (VBB) oblique seismometer and a 3-axis short period (SP) seismometer for partial redundancy and increase of the frequency range towards high frequencies (Lognonné and Pike 2015). These seismometers are located on a sensor assembly (SA) deployed directly on the ground, and connected to the electronic box (E-box) in the spacecraft by a tether; the SA also includes a leveling system (LVL) capable of tilting the SA for centering and calibrating purposes, and a thermal blanket (RWEB) for thermal isolation of the instruments. Besides the RWEB, the SA is also covered by a wind and thermal shield (WTS) protecting it from the external environment. Inspired by the data received from the Viking mission (Anderson et al. 1977), these protections were checked with encouraging results from simulations and tests done in the past (Lognonné et al. 1996, Nishikawa et al. 2014, Murdoch et al. 2017a, Mimoun et al. 2017).

In this paper, we will develop an active calibration procedure for SEIS to be executed on the Martian surface in order to determine in situ the gain of its instruments, and therefore to complement the calibrations made on Earth and the other calibrations made on Mars with calibration coils (see Lognonné et al. 2018 for more details). First, we complete the noise models developed in Mimoun et al. (2017) by focusing on noises at low frequency due to the instrument and the environment. Afterwards, we describe how SEIS was modeled for this study, and specify the different constraints we had to work with for designing the calibration procedure. Thirdly, using these completed noise models and the SEIS model, we show the method and the performance of the selected procedure. Then, an application of this calibration will be discussed.

2 Mars Seismic Noise

2.1 Previous Works

Noise models have already been developed for SEIS in previous studies, such as Lognonné and Mosser (1993), Pou et al. (2016), Murdoch et al. (2017a,b), Mimoun et al. (2017), Fayon et al. (2018). However, they were mainly focused on the nominal seismic range of SEIS between 0.01 Hz and 1 Hz (see Fig. 2), while other signals of scientific importance lie at lower frequencies (e.g. Van Hoolst et al. 2003), who only estimated the thermal noise), and low frequencies might have to be taken into account depending on the total duration of the calibration procedure. Thus, a more in-depth study is needed for determining the noise levels at very low frequency.
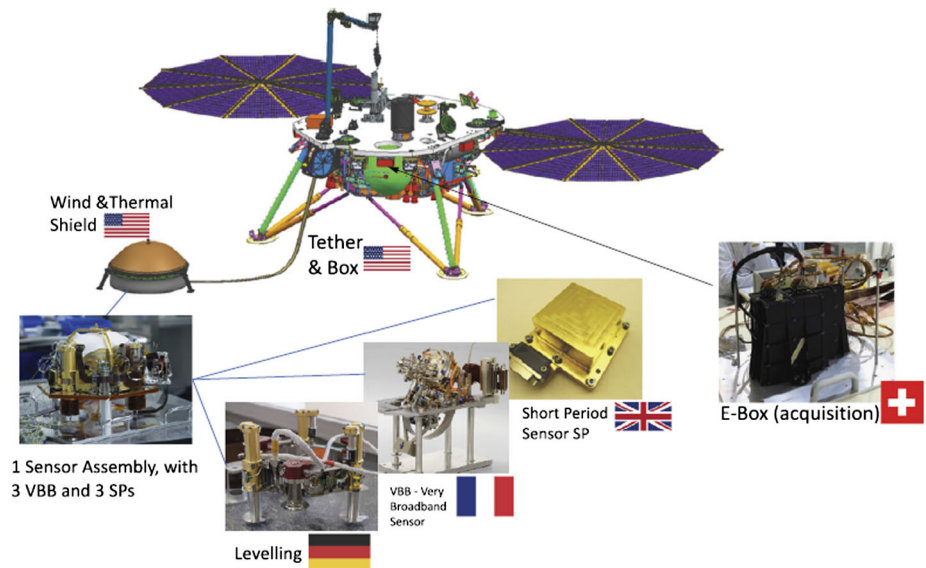
**Fig. 1** SEIS subsytems description (from Mimoun et al. 2017)

2.2 Thermal Noise at Low Frequency

Because of thermoelastic effects that change the geometric properties of the sensing elements of both VBBs and SPs, SEIS is sensitive to temperature fluctuations, and part of its output is due to this thermal signal (see Mimoun et al. 2017, Lognonné et al. 2018). Previous missions to Mars have shown (see Schofield et al. 1997, Clancy et al. 2000) that the day/night alternation is especially strong, and given that its frequency is at 1 Sol and its harmonics, the noise related to this alternation cannot be easily decorrelated from our tidal signals (Van Hoolst et al. 2003).

Here, we take the temperature measurements from MPF measurements (from Schofield et al. 1997), as MPF landed close to the Martian equator and the InSight landing site is also close to the equator. To match the sampling rate of our instruments, these data were interpolated to 1 Hz giving the temperature spectrum noise in Fig. 3, where the diurnal peak due to the day/night alternation are clearly visible.

We used the Pathfinder temperature in Fig. 3 as input to a simplified thermal model. The thermal model used here, in accordance with Mimoun et al. (2017), consists of two one-order low pass filters, one one-order filter representing the WTS with a time constant of 7.2 h and another one-order filter the sphere/RWEB around the VBBs with a time constant of 3 h. For the SP sensors, there is an additional one-order filter with a time constant of 460 s for a total of three filters. The time constants were determined from observed data recorded during noise tests campaigns as described in Mimoun et al. (2017). The Pathfinder temperature data was attenuated by the first two low pass filters to create the SCIT temperature (see Fig. 4), the most precise temperature measurements on 24 bits. However, due to the sphere, a additional phase delay has been observed between the SCIT temperature and the VBB temperature. The total phase delay between the two temperatures was estimated on the temporal data as a 10 hour delay at the day/night alternation frequency, meaning the variations seen by the SCIT temperature at this frequency are seen 10 hours later by the

Fig. 2 System L3 vertical noise estimates for daytime (top, a) and nighttime (bottom, b) environmental conditions for the VBBs. Horizontal solid lines represent the performance requirements (from Mimoun et al. 2017)
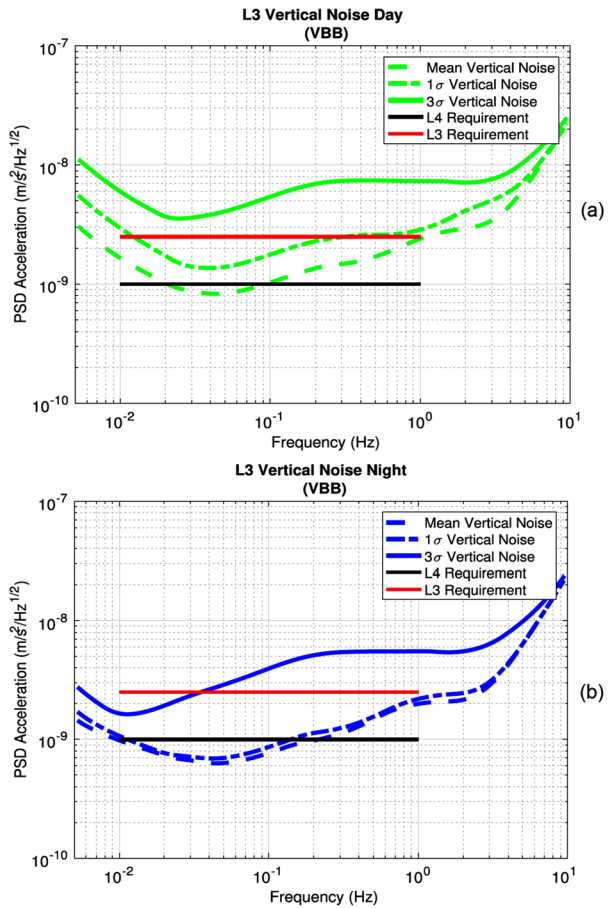

VBB inside the sphere. Variations at higher frequencies are phase-shifted due to both this phase delay and the thermal model with the low pass filters.

The VBB thermal sensitivity has been directly measured, with the current best estimates on the vertical axis being of 2.3×10^{-5} m s^{-2}/K, or 1.5×10^{-5} m s^{-2}/K along each VBB sensitivity axis (Mimoun et al. 2017). The thermal noise seen by the VBB is then derived by multiplying the temperature variations after filtering and the thermal sensitivity.

2.3 Pressure Noise Modeling at Low Frequency

Previous work by the InSight team has also been done for the pressure noise expected on Mars (Murdoch et al. 2017a,b). These simulations, based on LES simulations and spectral approaches, were however only made for frequency above 10^{-3} Hz, and therefore lack content at lower frequencies. Besides the ground acceleration previously mentioned, other effects grow significantly at lower frequency: Lognonné and Clévédé (2002) showed that an accelerometer also sees a free air gravity effect proportional to the ground displacement, and grows stronger at lower frequencies. Spiga et al. (2018) also considers the Newtonian attraction of the atmosphere as a direct upwards acceleration due to the air mass above the

Fig. 3 Temperature measurements from the Mars Pathfinder Lander (top, a) and its ASD (bottom, b). Measurements are taken at the top of the mast (1.0 m): since SEIS is on the ground, temperature variations might be larger for SEIS than these data. Data were downloaded through the Planetary Data System of NASA. The time interval taken was between Sol 18 and Sol 30 for having data as continuous and well-sampled as possible. One may pay attention to the spike at 1.1×10^{-5} Hz due to the day/night alternation, and the subsequent pikes as harmonics of this Martian daily variation. ASD is calculated from extrapolated temporal data over 3 years
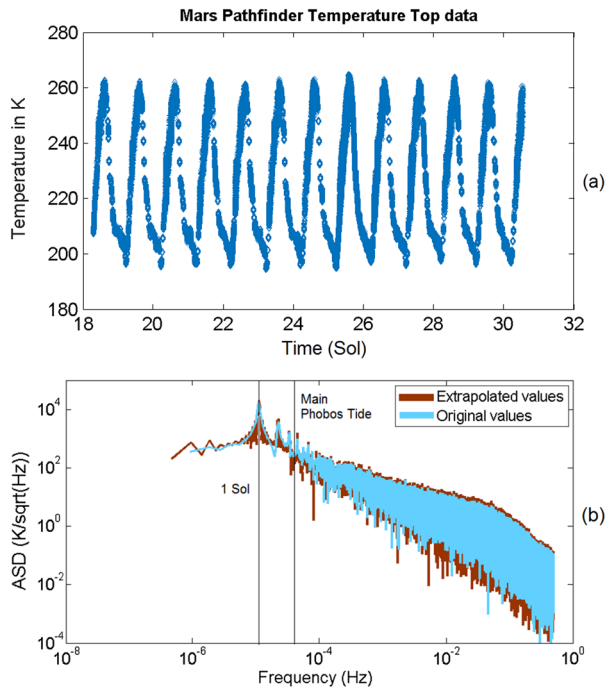
Fig. 4 SEIS design and protection for the instruments. The SCIT measurements is taken inside the RWEB, but outside the central sphere where the VBBs and SPs are. Source: CNES
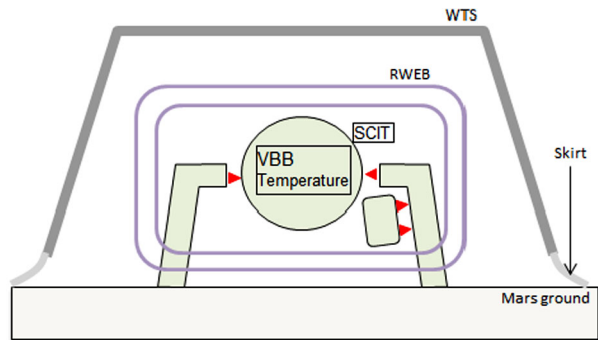
instrument. All three effects are taken into account in this paper, and are detailed in the following subsections.

Similar to what we did for the temperature, we use the pressure measurements taken from MPF measurements (Schofield et al. 1997) because of its proximity to the Martian equator similar to the landing site of InSight. To match the sampling rate of our instruments, these data were interpolated to 1 Hz giving the pressure spectrum noise in Fig. 5, where the diurnal peak due to the day/night alternation are clearly visible.

2.3.1 Atmospheric Loading

Murdoch et al. (2017b) showed that the pressure noise estimated is very close to the noise described in Sorrells (1971) for single point measurements: therefore, we choose here to

Fig. 5 Pressure measurements
from the Mars Pathfinder Lander
(top, a) and its ASD (bottom, b).
Because of glitches in the first,
more precise instrument with
range 6–10 mbar, we choose to
take the measurement of the
second instrument with a range
of 0–12 mbar. Data were
downloaded through the
Planetary Data System of NASA.
The time interval taken was
between Sol 18 and Sol 30 for
having data as continuous and
well-sampled as possible
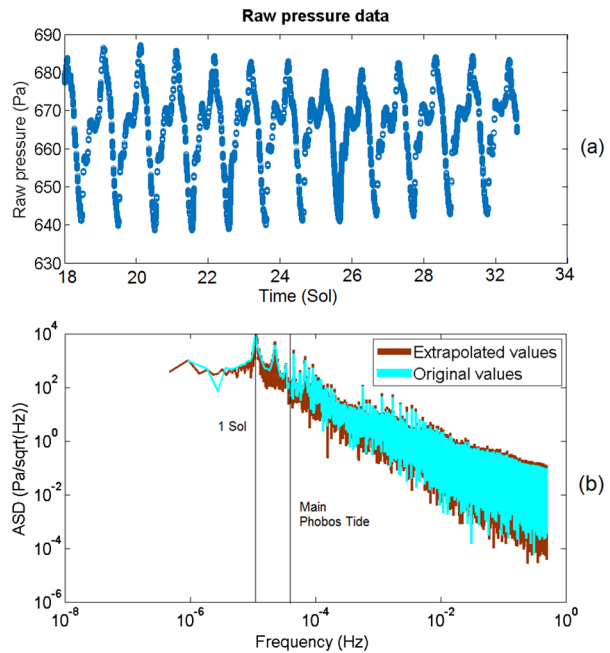
apply this method for estimating the atmosphere loading, being a low frequency pressure noise due to the pressure variations caused notably by winds, temperature variations, or atmospheric tides.

For the same reasons as the temperature, we used the pressure measurements taken from MPF measurements (see Fig. 5) and calculated the pressure noise with the formulae (from Sorrells 1971):

$$V = -i \frac{c}{\rho} \frac{v_p^2}{2v_s^2(v_p^2 - v_s^2)} P \qquad (1)$$

and

$$T = g\frac{V}{c} \qquad (2)$$

with c the wind speed, ρ the bulk density, v_p and v_s the seismic velocities, V the ground vertical velocity, P the pressure fluctuation, g the surface gravity and T the surface tilt. This surface tilt is induced by the ground vertical velocity, as this velocity generates a horizontal tilt seen by the VBB as a pressure noise (Murdoch et al. 2017b).

All parameter values are taken to fit with the models used in Murdoch et al. (2017b), with $v = 10\,\mathrm{m\,s^{-1}}$, $\rho = 1665\,\mathrm{kg\,m^{-3}}$, $v_p = 265\,\mathrm{m\,s^{-1}}$ and $v_s = 265\,\mathrm{m\,s^{-1}}$. When comparing our noise pressure spectrum (Fig. 6), our estimation shows a good match with the results in Murdoch et al. (2017b) at high frequency, and we do have an important signal at low frequency, especially around 1 Sol as expected because of the day/night alternation.

2.3.2 Free Air Gravity Effect

As mentioned in Lognonné and Clévédé (2002), an accelerometer at the surface of a planet sees more than the deflection and indentation of the ground due to atmospheric loading. Its
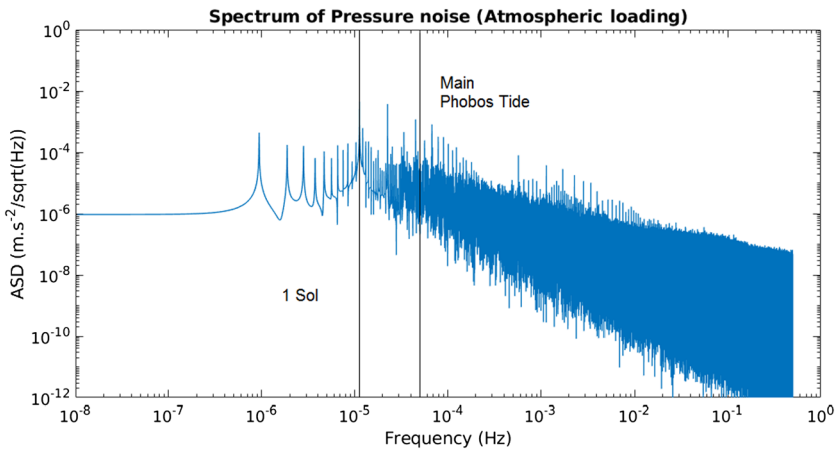
Fig. 6 ASD of pressure noise due to the atmospheric loading over 3 years, according to Murdoch et al. (2017b), from the MPF pressure measurements in Fig. 5. This spectrum is coherent with the ones calculated in Murdoch et al. (2017b) for frequencies between 10^{-3} and 10^{-1} Hz, and is higher for lower frequency due to the shorter duration of the simulations in Murdoch et al. (2017b) (thus underestimating low frequency noise)

measurements are also impacted by a free air gravity effect, an acceleration whose expression R_z on the vertical axis of the instrument is:

$$R_z = \frac{2u_r g}{r_{mars}} \tag{3}$$

where u_r is the radial displacement at the surface of the planet due to the atmosphere, and r_{mars} the radius of the planet, here being the radius of Mars. Since Sorrells (1971) gives us the velocity of the ground, we choose to integrate it in order to get the displacement of the ground and deduce from it the free air gravity effect. As seen in Fig. 7, its amplitude grows stronger than the velocity at low frequencies. Yet, at the diurnal frequency of 1.1×10^{-5} Hz, it still is weaker than the atmospheric loading.
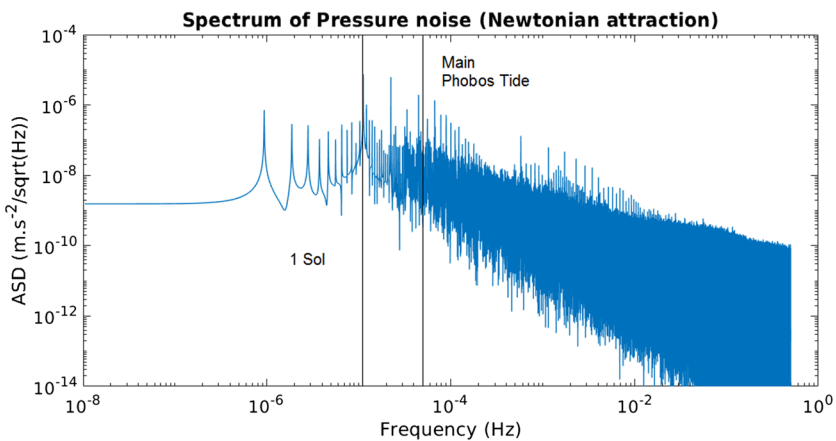
2.3.3 Newtonian Attraction

Besides its impacts on the ground velocity and displacement, the atmosphere also exerts a direct attraction on the seismometer as a body with a mass (Beauduin et al. 1996). This Newtonian attraction was quantified in Spiga et al. (2018) based on previous works from Warburton and Goodkind (1977) and Zürn and Widmer (1995) on Earth tidal science: the atmosphere is modeled as a uniform layer of air whose pressure is directly linked to its density, and therefore to its mass and its gravitational attraction by a coefficient:

$$A_n = -K_m P \tag{4}$$

where A_n is the Newtonian attraction, an acceleration along the vertical Z axis of the seismometer, and K_m the admittance value between the pressure P and the Newtonian attraction. At the surface of Mars, Spiga et al. (2018) estimates the admittance value to be around $12 \text{ nm s}^{-2} \text{ hPa}^{-1}$, which results in an ASD showed in Fig. 8
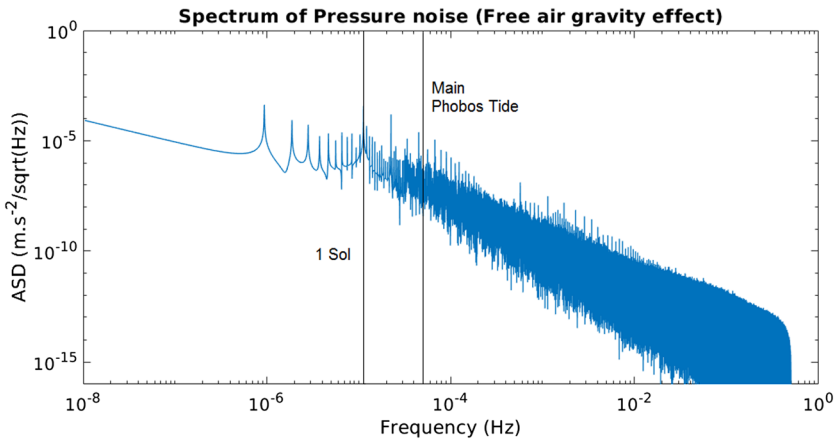
Fig. 7 ASD of pressure noise due to the free air gravity effect over 3 years, according to Lognonné and Clévédé (2002), from the MPF pressure measurements in Fig. 5. Besides the diurnal peak, another peak at lower frequency also became important
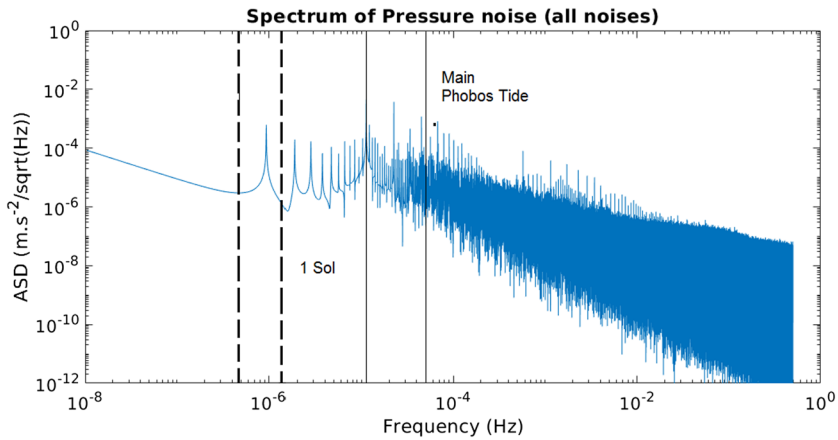

Fig. 8 ASD of pressure noise due to the direct Newtonian attraction of the Martian atmosphere over 3 years, according to Spiga et al. (2018), from the MPF pressure measurements in Fig. 5. Since this noise is also proportional to due the pressure, its shape is similar to the atmospheric loading noise seen in Fig. 5, but is significantly weaker

2.3.4 Total Pressure Noise

The total pressure noise spectrum is seen in Fig. 9, as the sum of the atmospheric loading, free air gravity effect and Newtonian attraction. Among the three, the dominating one is the atmospheric loading, with an amplitude at the diurnal frequency of $3.4 \times 10^{-3}\,\mathrm{m\,s^{-2}}/\sqrt{\mathrm{Hz}}$, compared to the $2.8 \times 10^{-4}\,\mathrm{m\,s^{-2}}/\sqrt{\mathrm{Hz}}$ of the free air gravity effect and $9.1 \times 10^{-6}\,\mathrm{m\,s^{-2}}/\sqrt{\mathrm{Hz}}$ of the Newtonian attraction. The free air gravity effect begins to become the dominant one at frequencies lower than 3.5×10^{-7} Hz, or periods higher than 33 Earth days, while the Newtonian attraction always stays weaker than the atmospheric loading.

Fig. 9 ASD of pressure noise due to the three contributions mentioned before (atmospheric loading, free air gravity effect, Newtonian atmosphere). The dotted lines indicate the dominant noise: on their left, the free air gravity effect is stronger, while on their right, the atmospheric loading is stronger. Between the two dotted lines, both are of similar strength

2.4 Other Noises

Also linked to atmospheric pressure, the impact of the mass redistribution on the local gravity due to the atmospheric loading was evaluated according to Lognonné and Clévédé (2002), but was found to be 10^5 times weaker than the free air gravity effect and thus was neglected.

Unlike the thermal noise and pressure noise which in previous studies were focused at higher frequency than the Sun and Phobos tidal signals, instrumental self-noise was constrained at low frequency during noise test campaigns done by IPGP and the Imperial College, with recordings during more than a week giving an upper bound on the self-noise since environmental noise during the tests are also impacting these recordings. Using them together with reference seismometers, it was possible to determine the self-noise of the VBB and the SP seismometers at low frequency.

Other noises were evaluated in accordance with the noise map outline drawn in Mimoun et al. (2017) (see Fig. 10). Thermoelastic tilt and tether noise have been studied using a finite element model of the instrument in Mimoun et al. (2017); the electric field noise is also studied in the appendix of the aforementioned paper. Magnetic noise have been modeled according to the theory described in Forbriger et al. (2010). Lander, WTS and HP3 induced noise are detailed in Murdoch et al. (2017a). Given their amplitude and standard variations (see Table 1), these noises were found low enough (Mimoun et al. 2017) to be neglected at low frequency compared to two main sources of noise: temperature and pressure, in the form of thermal noise and atmospheric loading.

3 Calibration of the SEIS Seismometer

3.1 Calibration Principle

The calibration of a seismometer consists of determining the relation between its input, the ground motion, and its output in the form of an electric signal (Wielandt 2013). While a
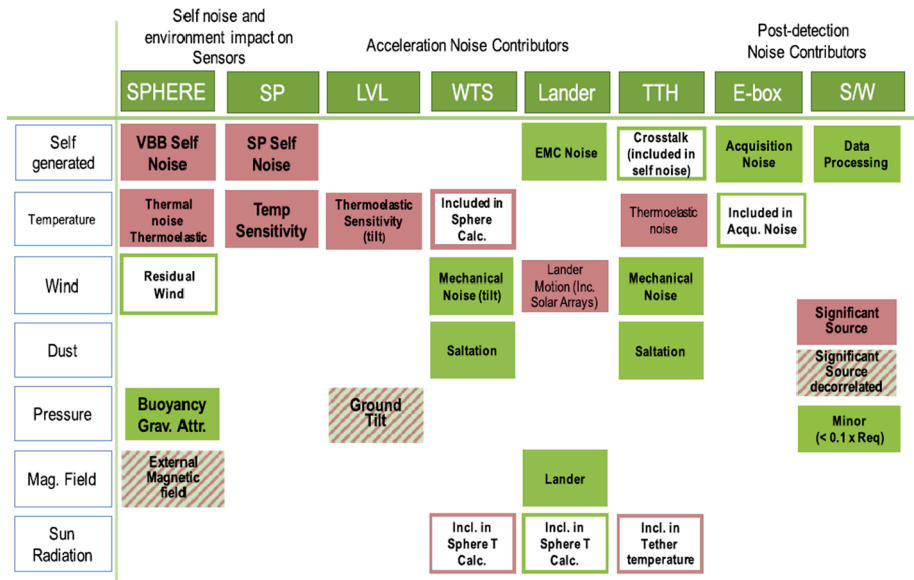
Fig. 10 Noise map outline from Mimoun et al. (2017). Expected dominant noises on the VBB are in dark color, minor sources of errors are in light color, and significant errors but that can be decorrelated by auxiliary sensors are in dashed dark/light color

Table 1 Comparison of all main noise sources. Max amplitude is peak-to-peak. The last two rows are the noise studied in this paper in the subsections before, and are clearly the dominant noises at low frequency (here, amplitudes are given at $1.1 10^{-5}$ Hz, the day/night alternation frequency)

Noise source	Max amplitude $m\,s^{-2}$	Standard variation $m\,s^{-2}$
Instrumental self noise	1.2×10^{-7}	1.2×10^{-8}
Electric noise	1.3×10^{-11}	9.5×10^{-14}
Magnetic noise	1.4×10^{-10}	2.6×10^{-11}
Thermal (high frequency) and thermoelastic noise	1.0×10^{-7}	4.2×10^{-9}
Hp3 noise	2.7×10^{-9}	3.1×10^{-10}
Tether noise	1.9×10^{-11}	2.0×10^{-12}
Lander noise	1.6×10^{-8}	1.4×10^{-9}
WTS noise	4.1×10^{-9}	1.8×10^{-10}
Pressure noise	3.4×10^{-6}	3.7×10^{-7}
Thermal noise (low frequency)	8.3×10^{-4}	8.7×10^{-5}

relative calibration, aimed at determining the frequency response shaping parameters, can be relatively easily done using the equivalence between ground acceleration and an external force on the seismic mass. It is possible to calibrate a seismometer by generating an electromagnetic force on the seismic mass to deduce the shape of the transfer function over the frequencies present in the electromagnetic signal generated. However, this method does not provide the absolute gain of the seismometer, and therefore an absolute calibration is more

difficult as it is needed to have in this case a precise knowledge of the ground motion used as input.

Several methods are available on Earth, like making use of well-known natural signals, such as ground noise (Pavlis and Vernon 1994) or local gravity (Anthony et al. 2018). However, such observables are not well-determined in our case for Mars: in fact, they are still intensively studied and modeled (Murdoch et al. 2017a,b; Mimoun et al. 2017), and measuring them with the precision expected from SEIS would greatly improve our knowledge on the Martian environment. Another possibility would be using a shaking table (Havskov and Alguacil 2004), but controlling perfectly the input generated by such a tool is not possible on Mars as it would require complex processing and extensive resources just for a single purpose; a cheaper and more convenient solution is to use the current structure of the instrument as best as we could to approximate a tilt table.

Therefore, we choose the solution to use the legs of the SEIS leveling system in order to create a tilt: as an accelerometer has an output proportional to the static acceleration, tilting it would create an effective force mainly in the horizontal direction, thus allowing us to determine the sensitivity of the seismometer (Havskov and Alguacil 2004). The tilt would be created by extending or shortening the legs of the sensor assembly depending on which seismometer is being calibrated. The current target on the precision of this procedure, detailed in Sect. 5 and in Panning et al. (2016) is a determination of the gain of the three VBBs in POS mode so that the gain of SEIS in the vertical Z axis (where the local gravity variations will be the strongest) is known with an accuracy of 0.35%, as it is the best currently possible within the one hour limit we set for it (explanations are given in the followings subsections).

3.2 Calibration Design

3.2.1 Leveling System

The leveling system (LVL) consists of two parts: a mechanical part, the leveling structure and the motor drive electronics (MDE) board. The leveling structure is mainly made of three legs, each with a linear actuator (LA) to either extend or retract them, supporting a structural ring on which the VBB and SP seismometers are mounted (Lognonné et al. 2018). These legs serve several purposes: getting the sensor assembly level, and providing mechanical coupling with the ground for better seismic recordings (Fayon et al. 2018). In this paper, another use of these legs will be made: the possibility to use them to create a tilt, and compare the response of the seismic sensors to this tilt as it would be done with a tilt table. The movement of a leg is quantified in quadsteps, with 5233 quadsteps equaling an elongation of 1 mm, and a maximum range for commands of 65 536 quadsteps: this provides a resolution and amplitude good enough for our purposes. However, because it works by steps, a direct drawback is the presence of hysteresis (or backlash): if moving the leg successively in two different directions, between the two movements, the linear actuator will activate without actually move the leg, because of empty space between the steps. The backlash amplitude was evaluated during tests at CNES in July 2016 at around 20 quadsteps of amplitude, which ended being too much. Thus, backlash had to be avoided for the whole calibration procedure.

The motor drive electronics (MDE) serves to command the linear actuators, and can also retrieve measurements from two independent tiltmeters on the supporting ring. But because of the sequential command structure used by the MDE, many constraints are added. For example, it is not possible to move the legs and take tiltmeters measurements at the same time. Also, it is not possible to move more than one leg at a given time. Because checkup

orders (communications between the motors and the lander to check their well-being) are necessary before and after each movement, a delay of about 3 s also have to be respected between each movement. Furthermore, the legs are commanded by reaching a given set speed for a given time: therefore, it is not possible to change the speed of one displacement, and a minimal and maximal speed have to be respected. A consequence of these constraints is for instance that sine waves are not possible, since it would require different speeds along a single displacement, with some of them being too slow for the linear actuator.

3.2.2 Absolute Gain Recovery

Using the LVL as a tilt table means that we had to study how to know the absolute amplitude of the tilt created by the legs displacements. While the MDE registers the number of steps done, the sand-like properties of the Martian soil (Delage et al. 2017) makes it not a good strategy for tilt recovery. It was first considered to use the high precision tiltmeters on the supporting ring, but they were found to be very highly sensitive to the temperature, to the point that the error in the deduced tilt only due to the temperature exceeded 2%, which is far too much for our goal.

Therefore, the solution chosen was to calibrate the VBB using the SP in order to make a relative calibration between the two seismometers, thus making the calibration an active (due to the legs moving) cross calibration between the VBB and the SP sensors: the tilt of the table will be estimated by the SP VEL output, and used to determine the difference between the gain of the SP and the gain of the VBB, as they will still see the tilt produced. If the difference is found to be the same (or close enough) as the difference that was found during absolute calibrations done on Earth, then we will assume that it is highly likely that the use of the on-Earth determined transfer functions for the VBB and the SP (detailed in Lognonné et al. 2018) will be acceptable. To increase the accuracy of the procedure, this calibration will be made at different temperatures on Mars: this will allow us to compare the impact of the temperature on the seismic sensors gains on Mars with its measured impact on Earth. The larger the temperature range is, the better the impact will be estimated. However, due to the limitations on the operational temperature of the LA, the procedure cannot be executed under $-35\,°C$.

3.2.3 VBB and SP Properties

For this study, we wanted to use both the VBB and the SP in their most precise mode. Therefore, the VBBs were used in scientific (SCI) mode (as opposed to engineering (ENG) mode) and position (POS) output (opposed to velocity (VEL) output), called VBB SCI POS, as it also allows to work at lower frequencies than any other modes, on 24 bits. The SP were used in velocity mode, called SP VEL, since its position output SP POS is only recorded on 12 bits while the SP VEL is recorded on 24 bits. Both seismometers are set at their highest gain (HG, high gain as opposed to LG, low gain) on Mars in order to calibrate the best resolution possible. The transfer function of the VBBs is given in Fig. 11: because of its shape, a calibration made at a frequency lower than 0.01 Hz is the most efficient in order to retrieve the gain of the transfer function on its flat part; higher frequencies gains can be calculated using the low frequency gain deduced from the low frequency absolute calibration and the transfer function shape deduced from relative calibrations. The nominal frequency acquisition for the VBB in this mode is at 1 Hz, and is at 100 Hz for the SP. More details on the VBB and SP functioning are given in Lognonné et al. (2018).

Fig. 11 Transfer function of VBB in SCI POS high gain (top, a) and SP in VEL high gain (bottom, b). Gain is in dB with respect to $1\ V/(m\,s^{-2})$. Model for the VBB transfer function was given by the IPGP team, while the SP transfer function comes from the Imperial College of London team. The vertical black line at the right in both transfer function is our Nyquist frequency for the simulations
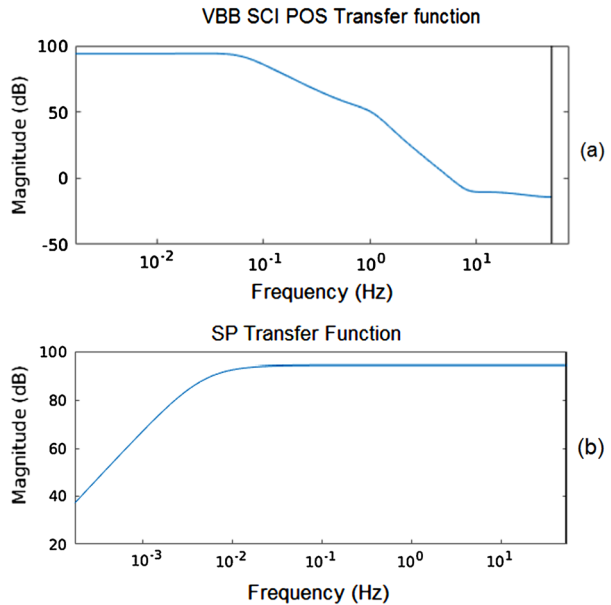
Because of the shape of the transfer functions, the tilt created is not a step function of time, but a periodic signal with a period chosen to be high enough to reach the VBB plateau, but low enough to be seen by the SPs as their transfer function is similar to a high pass filter for low frequency as seen in Fig. 11. In order to create a periodic signal while avoiding hysteresis issues, all motor actuations of the LA are done in the same direction, meaning that the legs are only either increasing or decreasing in a given calibration procedure. The amplitude of the leg movements is low enough to tilt the mechanical requirements on them, but the legs are moving fast enough to respect their minimum speed value. However, at this moving speed, the SP were prone to saturation: therefore, each rising edge is decomposed into 2 rising components in order to let the SP desaturate between them, and thus allowing a greater total tilt amplitude. Taking all of it into account, the period has been chosen at 112 s. The amplitude was determined to be as high as possible without reaching saturation on any of the sensor: due to the minimal speed requirement on the LAs, the movements are quite sharp and the SPs become the limiting factor because of how quickly they might reach saturation. In order to avoid it, the amplitude chosen is 0.002°, so that both VBBs and SPs on Mars can see the signal in their high gain mode (HG) for greater precision. The resulting tilt profile and how it is generated using the LA can be seen in Fig. 12.

3.2.4 Operational Constraints

Operational constraints were also taken into account for the design of this active cross calibration. Since all VBBs must be calibrated at the same time, the procedure duration must be within the wake-up duration of the lander. In order to make it possible, the absolute calibration procedure for all VBBs is designed to last less than 1 hour. Another constraint comes from the lowest temperatures on Mars: when the temperature falls below $-35°$, the linear actuators need heating in order to move. However, such heating create extremely high noise levels on SEIS, and thus are not compatible with the calibration purposes.
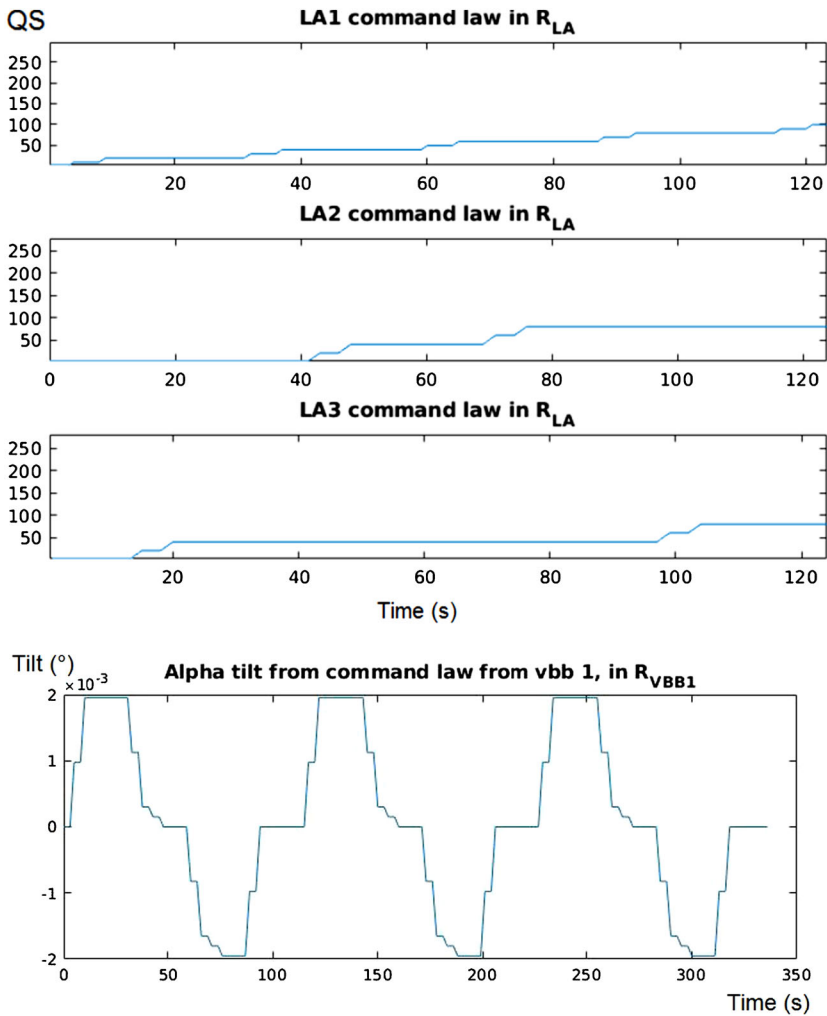
Fig. 12 Tilt profile generated by moving the LA (top, a) for the absolute calibration, seen by the VBB1 (bottom, b). Period is 112 s, amplitude is $2e^{-3}°$. Short delays before leg movement is 3 s, due to the wait for the checkup orders to be completed. In order to have a periodic signal, the legs must have the same extension at the end of each period: since the signal is rectangular, the period must therefore be a multiple of 4. Up to two legs can move per quarter period. If a leg must move during a given quarter period, it moves twice and each movement must last less than 2 s to avoid SP saturation. After the LA movements, 8 s were added to stabilize the VBB output and allow tiltmeter measurements that cannot be done during motor displacements, giving a quarter period of 28 s and thus a period of 112 s

As mentioned before, the impact of the temperature on the sensors gain must be known, thus the calibration must be done at several different temperatures to determine how their gains change depending on the temperature. Therefore, what is required for the calibration to efficiently retrieve the VBB gain is at least 3 complete calibrations of one hour: each at a different temperature and preferably as different as possible (for instance, max temperature, average temperature and lowest temperature possible before having to heat the linear actuators). In order to have the exact same conditions between VBBs in a given calibration
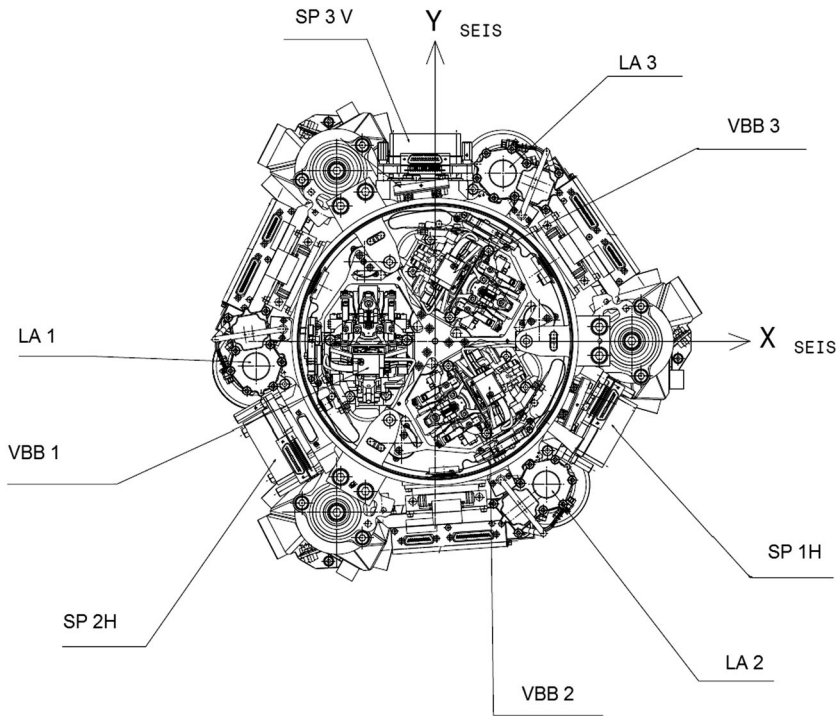
Fig. 13 SEIS sensor assembly with notably the position of the VBBs, SPs and positions of the legs and their motors (LA). SP H means horizontal SP, in opposition with the vertical SP V which is not used for this calibration procedure. Source: CNES

procedure, the whole calibration must be done in the same hour, and cannot be divided for instance as one half done at a given day, then the other half done the day after. As the calibration is designed not to saturate the output of all instruments, science recordings will still be done and exploitable even during the calibration procedure.

3.3 Active Cross Calibration Implementation

The current form of the active cross calibration is the following: calibration of 2 VBBs with a single tilt profile for 30 min, then calibration of the third one with another tilt profile for 30 min. The Fig. 13 gives the names of the different instruments used for the calibration. For the VBB 1 and 2, the tilt is generated by moving first the LA 1, then successively the LA 2 and LA 3. For the VBB 3, the tilt is generated by moving first successively the LA 1 and LA 3, and afterwards by moving successively the LA 1 and LA 2, as seen in Fig. 12. As the tilt is recorded by the VBBs in SCI POS HG mode, it is also recorded by the SPH 1 and 2 (horizontal SP) in VEL HG mode. Using both SPH, we reconstruct the real tilt of the sensor assembly and with a Fourier analysis, deduce the gain of the VBBs at the procedure period of 112 s.

3.4 Absolute Calibration Accuracy

In order to simulate the absolute calibration procedure, a code in Matlab has been developed, modeling the VBBs and their noise with Simulink models given by the IPGP and

Table 2 Accuracy of the calibration procedure on the gain deduction for each VBB, as relative error in %. The total gain in the z axis for SEIS is almost equal to $\frac{2}{3}(Gain_{vbb1} + Gain_{vbb2} + Gain_{vbb3})$. Results are worse for the calibration for VBB3 because it is the furthest from both SPH, resulting in a worse tilt reconstitution and thus transfer function estimation. Statistics are made on absolute values of errors relative to the theorical gain

Accuracy of the calibration procedure	VBB1 gain	VBB2 gain	VBB3 gain
Average accuracy	0.12	0.31	0.50
90th percile accuracy	0.22	0.48	0.76

Fig. 14 Accuracy (90th percile) of the calibration procedure on the Z axis of the VBB, relative to the theorical gain in %. The error on the Z axis is lower than the sum of the errors on each VBB gain because in most simulations, an error on the gain of one VBB is partially canceled by the error on another VBB (positive errors and negative errors)
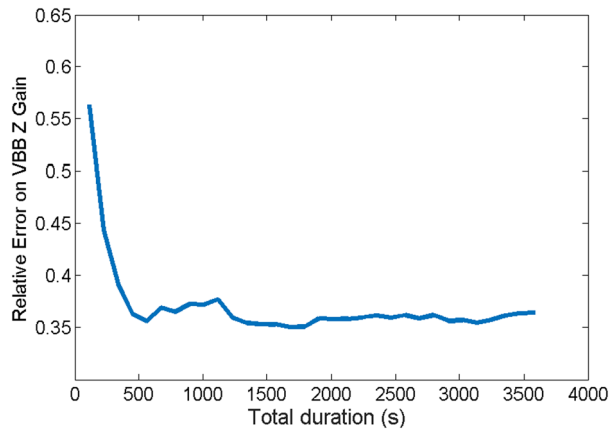
ISAE-Supaero teams, SPs with transfer function from the Imperial College teams and other instruments such as HP tiltmeters or LAs from data records from the CNES (Lognonné et al. 2018). The VBB model has been calibrated during tests at the Black Forest Observatory, at IPGP and also at CNES, while the SP transfer functions were calibrated during tests at the Imperial College and also at CNES. This code has been validated on several tests taken in July 2016, July–August 2017 and October 2017. The simulator was used running the calibration procedure 1000 times with random noises and initial conditions. The accuracy of the calibration was assessed by taking the Fourier transform of the input and simulated output signals, and comparing the obtained value with the real gain in the forward simulation at the frequency of the procedure profile. Results are given in Table 2, and temporal evolution is shown in Fig. 14.

It can be seen that for a total duration of one hour (twice half an hour) we manage to have an accuracy of 0.40% in 90% of the simulations on the resulting VBB vertical gain.

4 Application of the Active Cross Calibration Procedure

Several applications are possible using the results of the designed active cross calibration. Firstly, this calibration allows us to measure the gain of the VBB sensors relative to the SP sensors; by comparing the values to the ones measured on Earth, we can judge the well-being of SEIS and see how much the sensors have been altered during their journey to Mars. If the change is negligible, it is likely that SEIS did not suffer many alterations, and that calibrations done on Earth are still relevant. This would justify the use of the on-Earth

determined transfer function of both SP and VBB. As the absolute gains of the seismic sensors are known on Earth, it will be possible to convert their scientific outputs into real, physical values of the local gravity at the surface of Mars. Therefore, gravimetry will become possible and should be able to help us constrain the internal structure of Mars, with notably the detection of the Martian core state and size (Van Hoolst et al. 2003) by using the local gravity variations due to the Phobos. We will study the feasibility of such a approach in the following.

5 Current Knowledge of Mars Internal Structure

5.1 Current Models

Thanks to the various missions to Mars over more than half a century, our knowledge of Mars has arguably made it the best-known planet after the Earth. However, its internal structure has yet to be well-constrained due to the lack of pertinent observations. Among them, information on the crust can be deduced by joint inversion of topography and gravity field (e.g. Wieczorek and Zuber 2004). The chemical composition of Mars has been inferred from the composition of the SNC meteorites (McSween 1994), thought to be born from the mantle of Mars; this, coupled with mean density of Mars and measurements of the polar moment of inertia of Mars (Sohl and Spohn 1997, Zharkov and Gudkova 2005), models of thermal evolution for Mars (Rivoldini et al. 2011), and assumptions of precise chemical element ratio such as Fe/Si (Dreibus and Wanke 1985, Burbine and KM 2004) can help drawing a map of the interior of Mars. For the InSight mission, in order to prepare for tests and simulations before and after its arrival on Mars, several models of Mars have been studied in Panning et al. (2016) with for variations in the chemical composition, different thermal profiles (hot and cold case, from thermal evolution models) and presence of regolith at the surface.

Still, the core of Mars is only weakly impacted by the previous information. A stronger constrain for it comes from the tidal Love number k_2 (Rivoldini et al. 2011), which indicated that the core is at least partially liquid (Yoder et al. 2003). This deduction is also inferred by more recent values of the Love number k_2 deduced by data from the Mars Reconnaissance Orbiter (Genova et al. 2016), and is the case for models studied in Panning et al. (2016).

For this study, we use the same models as those used in Van Hoolst et al. (2003), with the reference model being the model A from Sohl and Spohn (1997). Because of the most recent values for k_2 and the deduced size of the core, the model A of Sohl and Spohn with a liquid core size $+200$ km (reaching a core size of 1668 km) is in accordance with more recent models such as Rivoldini et al. (2011) with a fully liquid core size of 1810 ± 153 km at 3 sigma for hot mantle models, and 1784 ± 159 km for cold mantle models (but can find model with solid inner core size at 1401 km). It is to be noted that these works use values for the Love number k_2 quite smaller than the most recent data ($k_2 = 0.159 \pm 0.009$ in Konopliv et al. 2011 whereas $k_2 = 0.1697 \pm 0.0009$ in Genova et al. 2016), which would mean an even larger liquid core: thus, this model serves as a worst case estimation. For instance, Panning et al. (2016) considers models where the size of the core varies less than this hypothesis, resulting in better results for the same accuracy in the gravimetric factor. The reference model is given in Table 3.

5.2 Available Observables for Enquiring the Internal Structure of Mars

While the value of the Love number k_2 can help constraining the state of the core (Yoder et al. 2003, Rivoldini et al. 2011), the InSight mission offers us another observable: the local

Table 3 Reference model description of Mars (Model A from Sohl and Spohn 1997). When the radius size of the core is changed, its density is modified to keep the same global mass of Mars

Boundary	Radius (km)	Pressure (GPa)	Temperature (K)	Density beneath (kg m^{-3})	Bulk modulus beneath (GPa)	Shear modulus beneath (GPa)
Physical surface	3390	0.00	210	2799	102.3	45.3
Crust-mantle boundary	3138	2.64	780	3493	130.7	69.3
Upper mantle–lower mantle boundary	2332	12.79	1775	3822	155.1	85.8
β-spinel-γ-spinel transition	1974	17.52	1853	4014	173.6	99.3
Core-mantle boundary	1667	21.75	1917	6772	145.5	87.3

gravity field on the surface, that could be measured by SEIS at low frequency when using it as a gravimeter (Lognonné et al. 2018). Indeed, for gravimetric calculations, we need to be able to see local gravity variations smaller than 10^{-8} m s^{-2} (Van Hoolst et al. 2003), which might be reachable over several years depending on the thermal noise encountered by the instrument and will be discussed later in Sect. 8. Calculations for the gravimetric factor of Mars linking the tidal potential of the Sun and Phobos have already been done taking into account the ellipsoidal shape of Mars (Lognonné et al. 1996), making it possible to deduced from possible internal models of Mars their gravimetric factor, and compare it with the deduced value by the InSight mission measurements over the mission duration (Van Hoolst et al. 2003).

Because the accuracy needed for resolving the main Phobos tide from the environmental noise is less strict than with the main Solar tide (Van Hoolst et al. 2003), we will focus our efforts at the main Phobos tide frequency of about 50 µHz. Assuming good results from the active cross calibration (see Sect. 3.1), we should know the exact gain at the Phobos main tide frequency, and thus the absolute value of its amplitude.

6 Phobos Tide Signal

6.1 Tide Modeling Assumptions

While we do aim at measuring the local gravity variations induced by the main Phobos tide at the surface of Mars, one must beforehand understand exactly what makes up a tidal signal. Basically, the Phobos tide here is a motion induced in the solid Mars by its moon Phobos, and the changes in its gravitational potential. Indeed, the surface motion is not the only signal that will be seen by SEIS: one must also take into account the direct attraction due to the passage of the celestial moon in the sky, the atmosphere loading, and environmental noises mentioned before (Agnew 2007). Non-tidal signals such as tectonics signals are ignored here since they typically are at higher frequencies than the Phobos tide signal. The combination of the vertical motion, the change in the Martian potential due to the tidal deformation and the direct attraction of Phobos gives the previously mentioned gravimetric factor gamma

calculated using the inner models of Mars at various frequencies (Van Hoolst et al. 2003, Lognonné et al. 1996) and updated with more recent values of the Mars Love numbers (from Genova et al. 2016, Konopliv et al. 2016). Atmosphere loading was discussed in Sect. 2.3 together with more considerations for environmental noises.

6.2 Signal Modeling

Here, we focus on the tide M_2 of Phobos which has the greatest amplitude among the tides induced by Phobos. As the main Phobos tide ($n = 2$, period of about 5.5 hr) is several times greater than the second largest one ($n = 3$, period of about 3.5 hr, see Van Hoolst et al. 2003), we will neglect other tidal signals from Phobos. However, the biggest tidal signal is in fact the semi-diurnal Solar tide: the Phobos main tide amplitude is only 8% of the Solar main tide amplitude. Still, because the main sources of noise on Mars will be the temperature and pressure noise, we expect to have high levels of noise close to the frequency of 1 Sol and its harmonics, making harder to resolve the tidal signal from the environmental noise for retrieving the gravimetric factor for the Solar main tide, since its frequency is at 1/2 Sol and therefore exactly at the first harmonic of the diurnal frequency.

We will therefore only consider as tidal signals the semi-diurnal Solar tide and the main 5.5 hr Phobos tide. The potential can be expressed as (Greff-Lefftz et al. 2005):

$$V_{M2} = -\frac{3}{4}\frac{GM}{a}\left(\frac{r_{mars}}{a}\right)^2 \sin^2(\theta + i)\cos\left(\frac{2\pi t}{T} + 2\phi + \Delta\psi\right) \tag{5}$$

With G the gravitational constant, M the mass of the attractor (either the Sun or Phobos), a the distance between the center of mass of Mars and the attractor, r_{mars} the distance between the center of mass of Mars and SEIS, i the inclination of the attractor's orbit, θ and λ the colatitude and longitude expected for SEIS on the Elysium Plains of 4.5° N and 135° E (Golombek et al. 2017), t the time, $\Delta\psi$ the phase of the attractor's orbit at initial time and T the respective period of the tide (1/2 Sol for the Sun main tide, 5 h 33 min for the Phobos main tide).

The potential is then derived into a gravitational acceleration, and gives the local gravity variation when multiplied by the gravimetric factor (Dehant et al. 1999, Agnew 2007). By deriving this potential, we get a gravity acceleration of:

$$g_{M2} = -\frac{3}{2}\frac{GM}{a^2}\left(\frac{r_{mars}}{a}\right)\sin^2(\theta + i)\cos\left(\frac{2\pi t}{T} + 2\phi + \Delta\psi\right) \tag{6}$$

And the local gravity variation Δg is deduced by multiplying this acceleration by the gravimetric factor γ, which in our case can be defined as the transfer function between the tidal force exerted along the perpendicular at the surface of Mars and the tidal gravity changes along the vertical as measured by a gravimeter (Dehant et al. 1999):

$$\Delta g = -\gamma g_{M2} \tag{7}$$

The sum of the local gravity variation due to the Sun main tide and the Phobos main tide gives a local gravity variation in the vertical Z axis which can be seen in Fig. 15. Here,

Fig. 15 Variations of the
Martian local gravity (mean
value of 3.71 m s^{-2}) due to both
the semi-diurnal Solar tide and
the semi-diurnal Phobos tide, the
biggest contributor being the
Solar tide (Phobos tide amplitude
being only 8% of this tide)
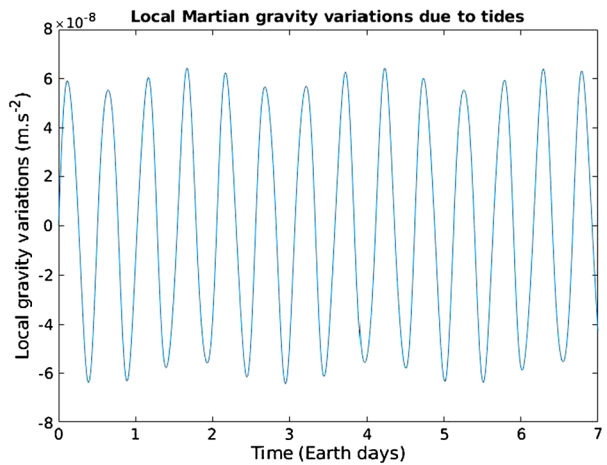
based on the values from Van Hoolst et al. (2003), we took a theoretical value of 1.05 for
the gravimetric factor.

Still, the signal measured by SEIS will not simply be these tidal gravity variations. The
output of SEIS will be the sum of these tidal signals, the environmental noises, the in-
strumental noises and other non-tidal signals such as tectonics signals (see Fig. 10). High
frequencies signals like quakes can be omitted since they can be filtered out with a low pass
filter. Since we want to know the amplitude of the tidal gravity variations, the main problem
will be the environmental noise, and especially the temperature and pressure noises studied
in Sect. 2. Therefore, we must be able to recover the signal related to the Phobos main tide
before being able to determine the gravimetric factor: such inversion is studied in the next
section.

7 Measurement Inversion Principle

7.1 Estimation of the SNR

From all noise sources studied in the previous section, it is possible to estimate how difficult
it will be to recover the tidal signals from the expected SEIS output on Mars. Working on
retrieving the local gravity variations, in this section, we will be working on the vertical
output of the VBB: with the thermal noise being the biggest contributor, the SNR before any
kind of treatment between the Phobos tide gravity variation amplitude and the environmental
noise amplitude seen by the VBB is close to 10^{-5}. Therefore, classical inversion methods
(such as Fourier transform or LMS decorrelation) cannot be used without improving the
SNR. Still, other fields are able to extract meaningful data from measurements with such
low levels of SNR, such as radar observations (Woodward 1953) and gravitational wave
astronomy (Schutz 1999). Inspired by the results in these fields, we studied the efficiency of
the matched filtering on our tidal signals: with the method described in this paper, in spite
of such SNR, we manage, depending on the noise on the temperature sensor, to recover the
tidal signals with an accuracy close to 0.1% in two years in the nominal case.

7.2 Matched Filtering

7.2.1 Principle

Matched filter is the optimal filter to improve the SNR in presence of a stochastic additive noise (Turin 1960): its principle is to study the correlation between our data with noise and a signal supposedly known in order to find the latter inside our data. Main applications include radar and GPS (Woodward 1953), where the signal sent is known, and must be found inside the response received later. It is also used in digital communications (Sklar 2001) to distinguish bit level in noisy signals and in astronomy (Schutz 1999) for detecting gravitational waves. For instance, assuming there is a signal whose shape is known either because we produce it (for a communication device such as GPS or radar) or using the theory (like gravitational waves or in our case, tidal signals) hidden in a noisy data sequence. By calculating the correlation C_{ys} between the noisy sequence (y) and our known signal (s):

$$C_{ys}(\tau) = \int_{-\infty}^{+\infty} y(t) * s(t - \tau) dt \tag{8}$$

The resulting correlation will reach a maximum when the start of the known signal matches its appearance inside the noisy sequence. By calculating the correlation in regard to time, we can determine the phase delay between the SCIT temperature and the thermal noise, caused by the temperature seen by the VBB. However, the exact amplitude still has to be extracted by another means like filtering since the position of the maximum correlation does not depend on amplitude. How we can apply it in our case is described in the following sections.

7.2.2 Application to Our Case

In our case, the tidal signals are mainly hidden by the thermal noise and the pressure noise. However, these noises are highly correlated respectively to the temperature and the pressure (Mimoun et al. 2017, Murdoch et al. 2017b), with the thermal noise being two order of magnitude higher than the pressure noise (see Table 1). Because of that, it is possible to use the matched filter to firstly eliminate the thermal noise, then to eliminate the pressure noise, leaving the tidal signals with the other less important noises so that the SNR is greatly improved. However, due to the instrumental noise of the pressure sensor and the temperature sensor for the InSight mission, such decorrelation is not perfectly possible and will result in an error in our tidal signals estimations. Noise models for the pressure sensor and the temperature sensor have been measured during tests campaigns and can be seen in Fig. 16. Notably, the self noise for the pressure sensor is much more important than the self noise measured for the temperature sensor, the latter being in fact almost a perfect white noise for a 24-bits sensor, with its range in the order of magnitude of 200 K. As a worst case, we also considered for our simulations the noise requirement on the temperature sensor as the sensor self noise, which is a lot noisier than the measured self noise.

In order to eliminate the thermal noise, two operations are necessary. First, the phase delay between the SCIT and the thermal noise must be retrieved. The matched filter is used classically for that, such as when it is used for radar operations: by correlating the noise data with the SCIT, the matched filter output shows maxima when the correlation is the highest, meaning when both signal are in phase, allowing us to determine the phasing between them. This process is shown in Fig. 17, where the matched filtering output is a phasing of 35 978 s
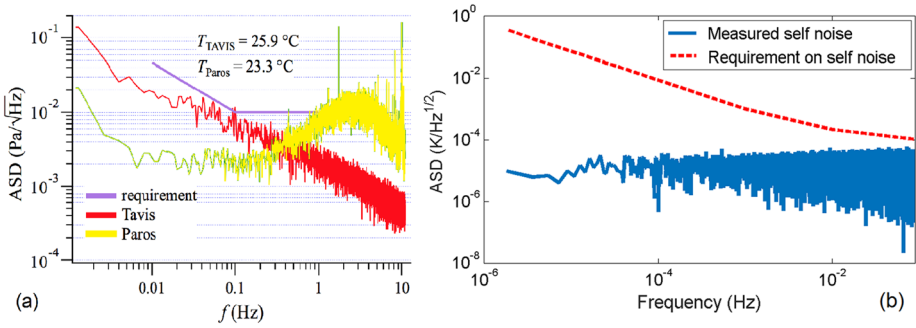
Fig. 16 Noise on the pressure sensor (left, a) and the temperature sensor (right, b) for the InSight mission. Values have been extrapolated to 10^{-8} Hz for the simulations. In order to have the worst case estimate, the noise on the Tavis pressure sensor has been taken in our simulations. For the temperature sensor, the worst case is studied by taking the requirements on its self noise (dashed line)
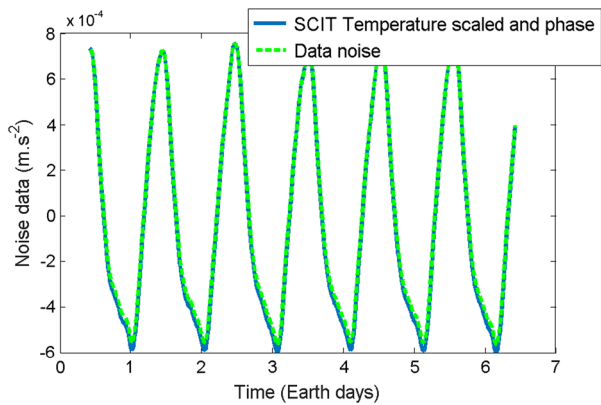
Fig. 17 Output of the matched filter between the data with noise and the SCIT measurements, when searching over a range of 24 h. The maximum correlation is given for 35 978 s, while the expected theoretical value is 36 000 s (10 h)
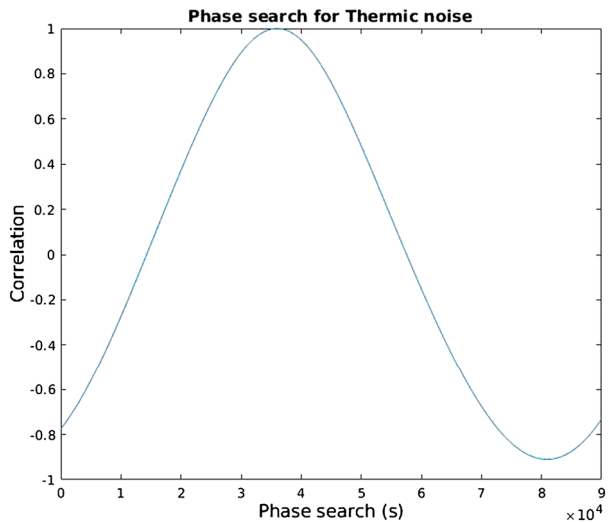

instead of the 36 000 s (10 h) expected, meaning an error on the phase of only 0.06% for 1 martian year.

After this phase operation, the residual is very similar to the SCIT temperature (see Fig. 18). Now, the VBB sensitivity must be calculated in order to eliminate the thermal noise from the noise data. If the thermal noise was substracted from the data in its entirety, the resulting residual would be dominated by the pressure noise, and thus be highly correlated to the pressure. Therefore, the thermal decorrelation applied here is to eliminate the thermal noise by using the temperature to maximize the correlation of the residual with the pressure. In practice, this means to find the best coefficients to be applied to the temperature that maximizes the correlation between 1. the difference between the vertical SEIS data and the function of temperature calculated by applying these coefficients to the temperature data, and 2. the pressure. Since our thermal noise (minus the phasing) is made to be equal to the temperature times the VBB sensitivity, in our case it means determining a single coefficient (the VBB sensitivity). This coefficient is then multiplied with the temperature data,

Fig. 18 Data with noise (dotted line) after phase correction from matched filtering compared to the SCIT measurements (solid line), scaled for visibility. The phase delay is significantly reduced. The difference between the two signals are mainly due to the temperature sensor noise, and the pressure noise

Fig. 19 Output of the matched filter between the noise data minus a searched vbb sensitivity factor times the SCIT, and the pressure measurements. The high spike corresponds to the value expected for the VBB thermal sensitivity
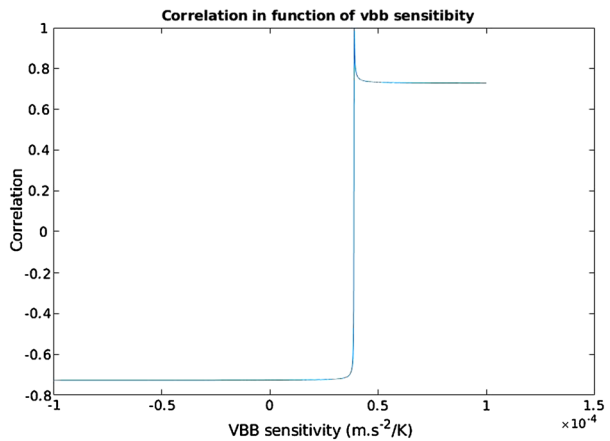
and the thermal noise decorrelation is done by subtracting this result from the vertical SEIS data. The main advantage of this method is to guarantee that pressure decorrelation will be possible afterwards since the residual will still be highly correlated to the pressure:

$$VBB_{sensitivity} = \max_{\alpha} \left| \int_{-\infty}^{+\infty} pressure(t) * diff(\alpha, t)dt \right| \tag{9}$$

$$diff(\alpha, t) = residual(t) - \alpha SCIT(t) \tag{10}$$

Where residual is the function shown in Fig. 18 (output of the matched filter on the phase between the data measurements from the VBB sensors and the SCIT), and α is the VBB thermal sensitivity. In this case, we want the maximum correlation in absolute value, since the noise and its related physical parameter may be anticorrelated like the pressure and the pressure noise (see Sect. 2.3). Here, the normalized correlation (between $+1$ and -1) between the residual and the pressure can be as high as 0.9999, showing the good results of our phase-based matched filter, but also the predominance of the thermal noise against the pressure noise.

The application of this method is shown in Fig. 19 and Fig. 20, where we can see that the residual is as expected very similar to the pressure after our filter (though this is mainly due

Fig. 20 Comparison between the residual of the noise data decorrelated with the SCIT measurements by our matched filter (top, a), by LMS filtering (middle, b), and the pressure (bottom, c). As expected after our matched filtering, the residual is highly correlated with the pressure measurements; However, for the LMS filtering, while the variance is lower, the residual is not very correlated with the pressure measurements
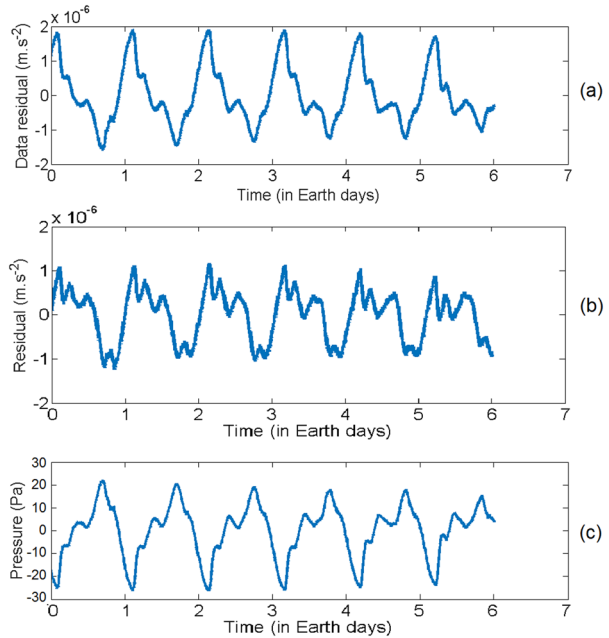
Fig. 21 Comparison between the residual of the noise data decorrelated with the SCIT measurements with LMS filtering (top, a) (see Fig. 20 b) and the same residual but after pressure decorrelation using an adaptive LMS filter as advised in Murdoch et al. (2017b) (bottom, b). The pressure decorrelation is not very effective here
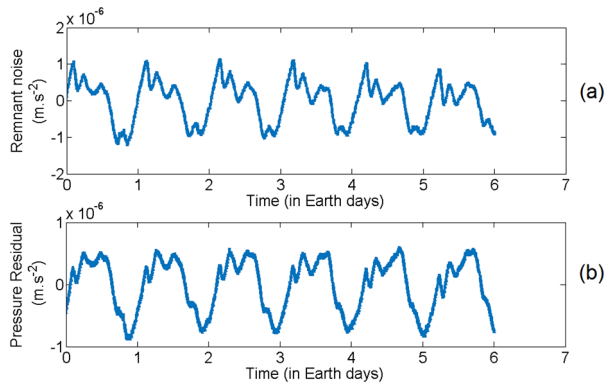

to the application of Sorrels' formula for the pressure noise), whereas classic decorrelation using for example an LMS adaptive filter, Monte-Carlo filtering or Levenberg-Marquardt filtering gives the result shown in Fig. 20; where the residual has indeed a lower variance but is very different from the pressure, and subsequent pressure decorrelation using for instance an adaptive LMS filter (advised as the best solution in Murdoch et al. 2017b) yields disappointing results in Fig. 21. This is because the temperature and the pressure are highly correlated, and deleting the thermal noise without extensive care can result in deleting signal similar to the temperature that was in fact part of pressure noise.

The same operation is done for the pressure noise, except there is a priori zero phase lag between the pressure and the pressure noise, and the useful signal expected to be highly correlated after our matched filter is the tidal signals, especially the Solar tide. However, Murdoch et al. (2017b) recommends using an adaptive LMS filter for decorrelating the pressure noise with the pressure, therefore both methods were tested. The results are shown in

Fig. 22 Comparison between the results of our decorrelation: top data (**a**) is after matched filtering on the temperature then LMS filtering on the pressure, while bottom data (**b**) is after matched filtering on the temperature then again matched filtering on the pressure. Both are very close with the tidal signals seen in Fig. 15
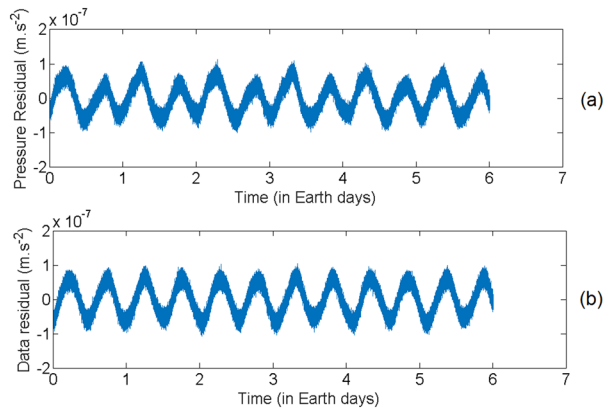
Fig. 23 Output of the matched filter when trying to extract the gravimetric factor from the main Solar tide. Because of the previous LMS decorrelations substracting signal from both the environmental noise at 1 Sol and its harmonic and the main Solar tide at 1/2 Sol, the results are pretty far for the theorical value of -1.05 (here, the value is about -0.8)
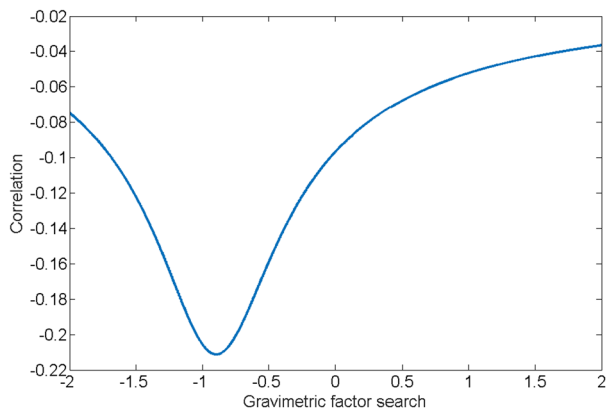

Fig. 22: it can be seen that both methods give really similar residuals. While it is possible to keep our matched filter approach for the pressure decorrelation, for the rest of the paper, we will work on the residual after an adaptive LMS filter to stay coherent with Murdoch et al. (2017b).

Now that the thermal and pressure noise are for the most part subtracted from the simulated data measurements, all that is left is the other noises seen by the VBB (self noise, magnetic noise, etc.) and the noises from the temperature and pressure sensors. Because their total amplitude is close to the tidal signals amplitude, we tested two methods to extract the gravimetric factor from the residuals: one is again a matched filter, where we try to maximize the correlation between the output of the matched filter and either the main Sun tide or the main Phobos tide, and the other one is a simple Fourier transform analysis at the main Phobos tide frequency. Results for the matched filter are shown in Fig. 23 and Fig. 24, while the final residual spectrum is shown in Fig. 25: when trying to retrieve the Solar tide, the gravimetric factor is very far from its theorical value, here taken at -1.05. This was expected, because the Solar tide is highly correlated with the thermal and pressure noise due to its main component being at 1 Sol, and therefore was partially lost during the decorrelation. However, the matched filter focused on the main Phobos tide gives better results, due to it being less affected by the previous decorrelations: unlike the main Solar tide, the main Phobos tide frequency does not match with any harmonics of the diurnal frequency.

Fig. 24 Output of the matched filter when trying to extract the gravimetric factor from the main Phobos tide. Results are better here than in Fig. 23 since the main frequency of the Phobos tide is far from the diurnal frequency of 1 Sol and its harmonics, thus less affected by the previous LMS decorrelations
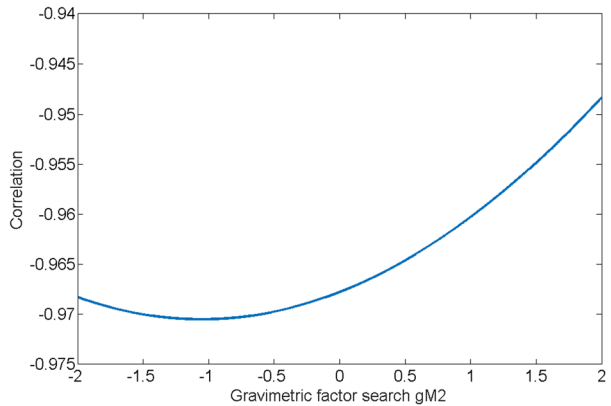
Fig. 25 Fourier transform of the residual in Fig. 22. Even after the decorrelations, a spike due to both the main Solar tide and the environmental noise is seen at 1/2 Sol (22 µHz). However, the main Phobos tide is also visible at 50 µHz
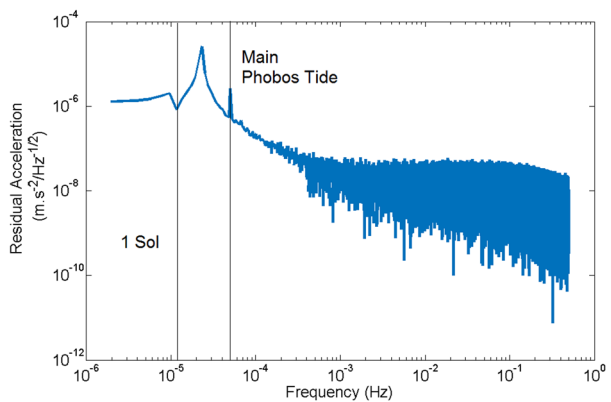
In most cases, this matched filter gives similar results than a Fourier analysis at the Phobos tide frequency (see Fig. 26).

7.2.3 Results

The results of the previous steps are shown in Fig. 26 for the different methods mentioned. In the end, both the Fourier analysis and matched filter are plausible methods for retrieving the gravimetric factor from the Phobos tide for the accuracy we desired after several months on Mars. The sensitivity to the noise on the temperature is also studied: while the measured noise gives quickly good results, this is not the case for the worst-case of the requirements that are not reaching 1% accuracy after three terrestrial years (one Martian year and a half), above the nominal InSight mission duration of two terrestrial year (one Martian year).

8 Sensitivity Study

The results shown in Fig. 26 assume that everything is known with perfect precision, and linear effects. Of course, this is not the case in reality: besides the inversion errors due to the noises seen by SEIS, other errors have to be taken into account. Only after estimating them all can we establish the true efficiency of our methods to estimate the gravimetric factor of
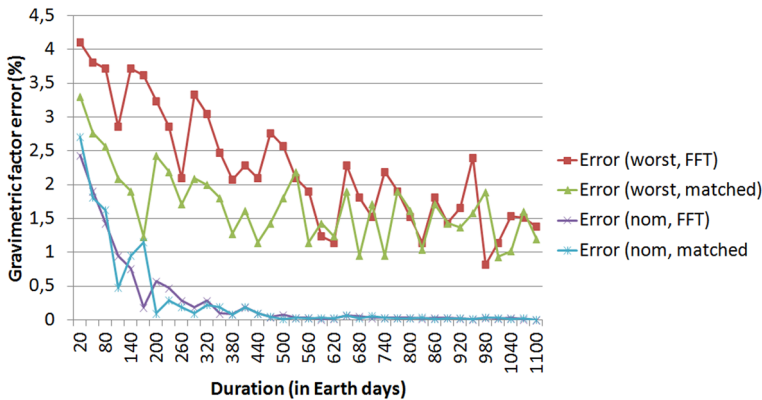
Fig. 26 Evolution of the relative error on the recovered gravimetric factor on the Phobos main tide depending on the method used, the noise of the temperature sensor (requirements or nominal) and the time. After 2 Martian years, the gravimetric factor is recovered in the worst case at 2.5%, and in the nominal case at better than 0.1%

Mars for the main Phobos Tide and thus how well the internal structure of Mars would be constrained.

8.1 Error Propagation

The essence of this paper is to determine the gravimetric factor by recovering the local gravity variations seen by SEIS. If these variations can be retrieved, then the gravimetric factor can be known by calculating the ratio between the variations and the tidal gravity variation due to Phobos, derived from its tidal potential. As such, the gravimetric factor γ is calculated as followed (see Eq. (7)):

$$\gamma = -\frac{\Delta g}{g_{M_2 Phobos}} \tag{11}$$

where Δg is the local gravity variations, and $g_{M_2 Phobos}$ is the tidal gravity variation due to the main tide of Phobos. The latter expression is given in Eq. (6). On the other hand, Δg is deduced from the SEIS output, and therefore is a function of its gain:

$$\Delta g = \frac{Output_{SEIS}}{Gain_{SEIS}} \tag{12}$$

where $Output_{SEIS}$ is the output returned by SEIS, thus the data measurements acquired, and $Gain_{SEIS}$ the absolute gain of SEIS calculated from the active cross calibration described in Sect. 3. Using all the previous equations, the complete expression for the calculation of the gravimetric factor is:

$$\gamma = -\frac{Output_{SEIS}}{Gain_{SEIS} * (-\frac{3}{2}\frac{GM}{a^2}(\frac{r_{mars}}{a})) * (\sin(\theta + i)^2) * \cos(2\pi t/T + 2\phi + \Delta\psi))} \tag{13}$$

Equation ([13]) is then derived to determine the worst total error on the gravimetric factor:

$$\frac{\Delta\gamma}{\gamma} = \frac{\Delta Output_{SEIS}}{Output_{SEIS}} + \frac{\Delta Gain_{SEIS}}{Gain_{SEIS}}$$

$$+ \frac{\Delta(GM)}{GM} + \frac{\Delta r_{mars}}{r_{mars}} + 3 * \frac{\Delta a}{a}$$

$$2 + 2 * \frac{\Delta(\sin(\theta + i))}{\sin(\theta + i)} + \frac{\Delta(\cos(2\pi t/T + 2\phi + \Delta\psi))}{\cos(2\pi t/T + 2\phi + \Delta\psi)} \qquad (14)$$

The first term refers to our decorrelation process detailed in Sect. 7. The second term is the error determined in Sect. 3. All five others are linked to the ephemerides of Phobos and Mars, and to the actual position of SEIS and the InSight lander on Mars.

8.2 Error Determination

While the error due to our decorrelation process depends on the time spent on accumulating data (see Sect. 7 and Fig. 26), the other errors present in Eq. (14) can be evaluated beforehand. Firstly, the error on the SEIS gain was already studied in Sect. 3: we can take the value of 0.4%.

Secondly are the terms due to the position of SEIS on Mars (namely the longitude ϕ, colatitude θ and distance r_{mars} between Mars and SEIS): thanks to the orbiters present (for instance Mars Express, Mars Odyssey or Mars Reconnaissance Orbiter), it will be possible after the landing of InSight to map its actual position on the surface of Mars and therefore determine the aforementioned parameters. Notably, HiRiSE aboard Mars Reconnaissance Orbiter can reach a resolution of 0.25 m/px (McEwen et al. 2010). When scaled to the mean Martian radius, this means an error of less than 1×10^{-5}% on the longitude and colatitude. Similarly, the error on the radius is less than 1×10^{-4}% with our current topography models of Mars (Seidelmann et al. 2007). Therefore, these position errors are highly negligible before the error on the gain determination of SEIS.

Thirdly, we have to assess the errors on the Phobos ephemerides, namely its mass, distance to Mars, inclination, period and declination (taken into account in the $\Delta\Psi$ term). Recent flybys by Mars Express around Phobos give an estimation of its mass down to 1.5% error (Pätzold et al. 2014), but this very conservative error is also due to distant flybys being taken into account: close flybys rather give estimates down to 0.3% error on the mass (Andert et al. 2010), and secular evolution models of the orbit of Phobos can even reduce it to less than 0.1% (Rosenblatt et al. 2008, Konopliv et al. 2006). Using these mass values, ephemerides of Phobos have been refined, with an error on the distance between Phobos and Mars down to 2 km and 30 millidegrees for the inclination and declination, meaning relative errors of 0.03% on the distance and 0.04% on the angles (Jacobson et al. 2018). If we choose to taken into account the middle ground of the solutions with the close flybys only, this leads to a total error due to the Phobos ephemerides around 0.5%. These errors might also be further reduced with future planned missions to Phobos such as MMX (Campagnola et al. 2018).

8.3 Expected Results

All the errors discussed in the previous section (Sect. 8.2) accounts for a total fixed error of 1% on the gravimetric factor, plus the error due to the inversion method in Sect. 7. Using

Table 4 Efficiency of the procedure over time. For the inversion process, the first error is if the temperature sensor noise is equal to the self noise requirement, and the second one is if the temperature sensor noise is only its electronic bit noise as measured

Time	Error on SEIS gain	Error on position of SEIS	Error on Phobos ephemerides	Inversion process	Total accuracy
6 months	0.4%	≤0.01%	0.5%	4% or 1%	5.9% or 1.9%
1 year	0.4%	≤0.01%	0.5%	3% or 0.25%	3.9% or 1.15%
2 year	0.4%	≤0.01%	0.5%	2.5% or 0.1%	3.4% or 1.0%

Table 5 Accuracy needed for Mars knowledge improvement, based on Van Hoolst et al. (2003). With the current state of knowledge on the Phobos ephemerides and the calibration procedure chosen, the state of the core can be determined, but its size is not accurately known

Constrains on the Martian core	Accuracy needed (Van Hoolst et al. 2003)	Current results
State of the core	1.2%	Valid in one year
Size of the core (at 200 km)	0.6%	Need refinement on the Phobos ephemerides
Size of the core (at 100 km)	0.3%	Not guaranteed for the current calibration procedure

the values shown in Fig. 26 and the gravimetric factor values in Van Hoolst et al. (2003), it is possible to estimate the time needed to constrain the internal structure of Mars. These estimates are shown in Table 4 and Table 5: if we take the absolute worst case (the noise on the temperature sensor being equal to its requirement), then even after 2 years, the gravimetric factor is not retrieved accurately enough to constrain the internal structure of Mars. However, in the nominal case with the sensor noise being as low as measured, equal to a electronic bit noise, it might be possible after two years to deduce the state of the core from the local gravity variations measured by SEIS.

Indeed, for a given internal model of Mars such as the model A of Sohl and Spohn, it is possible with our method to resolve the gravity variations caused by a liquid core from those caused by a solid core of the same size, as a liquid core would create local gravity variations about 1.2% higher than the variations from a solid core (Van Hoolst et al. 2003), a difference lower than our error budget of 1% over two years. This method is also useful when working with several models: Panning et al. (2016) showed that with a precision better than 0.5% on the VBB absolute gain, the gravimetric factor can discriminate between models with similar seismic waves travel time (notably ScS waves) but with different core sizes. Since this paper reached a precision of 0.4% on the VBB absolute gain plus an error of 0.1% over two years on the gravimetric factor recovery, using a priori models coupled with other methods such as seismic events could allow us to constrain both the state and the size of the Martian core. This performance can be improved if the error on the Phobos ephemerides, independent of the InSight mission, are improved in the following years, or if the calibration on the SEIS gain gets more precise.

9 Conclusion

In this paper, we improved the previous noise models of SEIS from Mimoun et al. (2017) with a more in-depth study at low frequency. Using them, we designed an active cross calibration between the VBB and SP sensors, taking into account all constraints from the LVL system, the instruments respective transfer function, tilt recovery issues and operational constraints. Depending on the result of this active cross calibration, determination of the absolute gain of the VBB might be possible, which would open the way to the study of gravimetric signals such as the main Phobos tide: to study this possibility, we implemented the tidal signal of the main Phobos tide and the main Solar tide, those two being the biggest tidal signals on Mars. Then, from the implemented signal together with our new noise models, we developed a method based on matched filters for retrieving the gravimetric factor, and studied the evolution of the error on this recovery versus the time needed to accumulate the data. Finally, we studied the error propagation, with the main error sources being the calibration on the SEIS gain, the error on the Phobos ephemerides and the inversion process with the decorrelations. The results show that it might be possible for SEIS to constrain the state of the core during its nominal lifetime of 2 terrestrial years.

References

D.C. Agnew, Earth tides, in *Treatise on Geophysics*, vol. 3 (Elsevier, Amsterdam, 2007), pp. 163–195

D.L. Anderson, W.F. Miller, G.V. Latham, Y. Nakamura, M.N. Toksöz, A.M. Dainty, F.K. Duennebier, A.R. Lazarewicz, R.L. Kovach, T.C.D. Knight, Seismology on Mars. J. Geophys. Res. **82**(28), 4524–4546 (1977). https://doi.org/10.1029/JS082i028p04524

T.P. Andert, P. Rosenblatt, M. Pätzold, B. Häusler, V. Dehant, G.L. Tyler, J.C. Marty, Precise mass determination and the nature of Phobos. Geophys. Res. Lett. **37**(9) (2010). https://doi.org/10.1029/2009GL041829

R.E. Anthony, A.T. Ringler, D.C. Wilson, Improvements in absolute seismometer sensitivity calibration using local Earth gravity measurementsshort note. Bull. Seismol. Soc. Am. **108**(1), 503–510 (2018). https://doi.org/10.1785/0120170218

R. Beauduin, P. Lognonné, J.P. Montagner, S. Cacho, J.F. Karczewski, M. Morand, The effects of the atmospheric pressure changes on seismic signals or how to improve the quality of a station. Bull. Seismol. Soc. Am. **86**(6), 1760 (1996)

T.H. Burbine, K.M. O'Brien, Determining the possible building blocks of the Earth and Mars. Meteorit. Planet. Sci. **39**(5), 667–681 (2004). https://doi.org/10.1111/j.1945-5100.2004.tb00110.x

S. Campagnola, C.H. Yam, Y. Tsuda, N. Ogawa, Y. Kawakatsu, Mission analysis for the Martian Moons Explorer (MMX) mission. Acta Astronaut. **146**, 409–417 (2018). https://doi.org/10.1016/j.actaastro.2018.03.024

R.T. Clancy, B.J. Sandor, M.J. Wolff, P.R. Christensen, M.D. Smith, J.C. Pearl, B.J. Conrath, R.J. Wilson, An intercomparison of ground-based millimeter, MGS TES, and Viking atmospheric temperature measurements: seasonal and interannual variability of temperatures and dust loading in the global Mars atmosphere. J. Geophys. Res., Planets **105**(E4), 9553–9571 (2000). https://doi.org/10.1029/1999JE001089

V. Dehant, P. Defraigne, J.M. Wahr, Tides for a convective Earth. J. Geophys. Res., Solid Earth **104**(B1), 1035–1058 (1999). https://doi.org/10.1029/1998JB900051

P. Delage, F. Karakostas, A. Dhemaied, M. Belmokhtar, P. Lognonné, M. Golombek, E.D. Laure, K. Hurst, J.C. Dupla, S. Kedar, Y.J. Cui, B. Banerdt, An investigation of the mechanical properties of some martian regolith simulants with respect to the surface properties at the InSight mission landing site. Space Sci. Rev. **211**(1–4), 191–213 (2017). https://doi.org/10.1007/s11214-017-0339-7

G. Dreibus, H. Wanke, Mars, a volatile-rich planet. Meteoritics **20**, 367–381 (1985)

L. Fayon, B. Knapmeyer-Endrun, P. Lognonné, M. Bierwirth, A. Kramer, P. Delage, F. Karakostas, S. Kedar, N. Murdoch, R.F. Garcia, N. Verdier, S. Tillier, W.T. Pike, K. Hurst, C. Schmelzbach, W.B. Banerdt, A numerical model of the SES leveling system transfer matrix and resonances: application to SEIS rotational seismology and dynamic ground interaction. Space Sci. Rev. (2018)

T. Forbriger, R. Widmer-Schnidrig, E. Wielandt, M. Hayman, N. Ackerley, Magnetic field background variations can limit the resolution of seismic broad-band sensors. Geophys. J. Int. **183**(1), 303–312 (2010)

A. Genova, S. Goossens, F.G. Lemoine, E. Mazarico, G.A. Neumann, D.E. Smith, M.T. Zuber, Seasonal and static gravity field of Mars from MGS, Mars Odyssey and MRO radio science. Icarus **272**, 228–245 (2016). https://doi.org/10.1016/j.icarus.2016.02.050

M. Golombek, D. Kipp, N. Warner, I.J. Daubar, R. Fergason, R.L. Kirk, R. Beyer, A. Huertas, S. Piqueux, N.E. Putzig B.A. Campbell, G.A. Morgan, C. Charalambous, W.T. Pike, K. Gwinner, F. Calef, D. Kass, M. Mischna, J. Ashley, C. Bloom, N. Wigton, T. Hare, C. Schwartz, H. Gengl, L. Redmond, M. Trautman, J. Sweeney, C. Grima, I.B. Smith, E. Sklyanskiy, M. Lisano, J. Benardini, S. Smrekar, P. Lognonné, W.B. Banerdt, Selection of the InSight landing site. Space Sci. Rev. **211**(1–4), 5–95 (2017). https://doi.org/10.1007/s11214-016-0321-9

M. Greff-Lefftz, L. Métivier, H. Legros, Analytical solutions of love numbers for a hydrostatic ellipsoidal incompressible homogeneous Earth. Celest. Mech. Dyn. Astron. **93**(1–4), 113–146 (2005). https://doi.org/10.1007/s10569-005-6424-3

J. Havskov, G. Alguacil, *Instrumentation in Earthquake Seismology*. Modern Approaches in Geophysics (Springer, Berlin, 2004)

R. Jacobson, A. Konopliv, R. Park, W. Folkner, The rotational elements of Mars and its satellites. Planet. Space Sci. **152**, 107–115 (2018). https://doi.org/10.1016/j.pss.2017.12.020

A.S. Konopliv, C.F. Yoder, E.M. Standish, D.N. Yuan, W.L. Sjogren, A global solution for the Mars static and seasonal gravity, Mars orientation, Phobos and Deimos masses, and Mars ephemeris. Icarus **182**(1), 23–50 (2006). https://doi.org/10.1016/j.icarus.2005.12.025

A.S. Konopliv, S.W. Asmar, W.M. Folkner, O. Karatekin, D.C. Nunes, S.E. Smrekar, C.F. Yoder, M.T. Zuber, Mars high resolution gravity fields from MRO, Mars seasonal gravity, and other dynamical parameters. Icarus **211**(1), 401–428 (2011). https://doi.org/10.1016/j.icarus.2010.10.004

A.S. Konopliv, R.S. Park, W.M. Folkner, An improved JPL Mars gravity field and orientation from Mars orbiter and lander tracking data. Icarus **274**, 253–260 (2016). https://doi.org/10.1016/j.icarus.2016.02.052

P. Lognonné, E. Clévédé, *Normal Modes of the Earth and Planets*. International Geophysics, vol. 81, p. 125 (2002)

P. Lognonné, B. Mosser, in *Planetary Seismology*. Surveys in Geophysics, vol. 14 (1993), pp. 239–302. https://doi.org/10.1007/BF00690946

P. Lognonné, W.T. Pike, Planetary seismometry, in *Extraterrestrial Seismology* (Cambridge University Press, Cambridge, 2015), pp. 36–50. https://doi.org/10.1017/CBO9781107300668.006

P. Lognonné, J.G. Beyneix, W.B. Banerdt, S. Cacho, J.F. Karczewski, M. Morand, Ultra broad band seismology on InterMarsNet. Planet. Space Sci. **44**(11), 1237–1249 (1996). https://doi.org/10.1016/S0032-0633(96)00083-9

P. Lognonné, W.B. Banerdt, D. Giardini, W.T. Pike, U. Christensen, P. Laudet, S. de Raucourt, P. Zweifel, S. Calcut, M. Bierwirth, K. Hurst, F. Ljpelaan, J. Umland, R. Llorca Cejudo, S. Larson, R.F. Garcia, S. Kedar, B. Knapmeyer-Endrun, D. Mimoun, A. Mocquet, M. Panning, R. Weber, A. Sylvestre-Baron, G. Pont, N. Verdier, L. Kerjean, T. Hoffman, J. Willis, S. Smrekar (the SEIS Team), SEIS: The Seismic Experiment for Internal Structure of InSight. Space Sci. Rev. (2018, submitted)

A.S. McEwen, M.E. Banks, N. Baugh, K. Becker, A. Boyd, J.W. Bergstrom, R.A. Beyer, E. Bortolini, N.T. Bridges, S. Byrne, B. Castalia, F.C. Chuang, L.S. Crumpler, I. Daubar, A.K. Davatzes, D.G. Deardorff, A. DeJong, W.A. Delamere, E.N. Dobrea, C.M. Dundas, E.M. Eliason, Y. Espinoza, A. Fennema, K.E. Fishbaugh, T. Forrester, P.E. Geissler, J.A. Grant, J.L. Griffes, J.P. Grotzinger, V.C. Gulick, C.J. Hansen, K.E. Herkenhoff, R. Heyd, W.L. Jaeger, D. Jones, B. Kanefsky, L. Keszthelyi, R. King, R.L. Kirk, K.J. Kolb, J. Lasco, A. Lefort, R. Leis, K.W. Lewis, S. Martinez-Alonso, S. Mattson, G. McArthur, M.T. Mellon, J.M. Metz, M.P. Milazzo, R.E. Milliken, T. Motazedian, C.H. Okubo, A. Ortiz, A.J. Philippoff, J. Plassmann, A. Polit, P.S. Russell, C. Schaller, M.L. Searls, T. Spriggs, S.W. Squyres, S. Tarr, N. Thomas, B.J. Thomson, L.L. Tornabene, C.V. Houten, C. Verba, C.M. Weitz, J.J. Wray, The High Resolution Imaging Science Experiment (HiRISE) during MRO's Primary Science Phase (PSP). Icarus **205**(1), 2–37 (2010). https://doi.org/10.1016/j.icarus.2009.04.023

H.Y. McSween, What we have learned about Mars from SNC meteorites. Meteoritics **29**(6), 757–779 (1994). https://doi.org/10.1111/j.1945-5100.1994.tb01092.x

D. Mimoun, N. Murdoch, P. Lognonné, K. Hurst, W.T. Pike, J. Hurley, T. Nébut, W.B. Banerdt, The noise model of the SEIS seismometer of the InSight mission to Mars. Space Sci. Rev. **211**, 383–428 (2017). https://doi.org/10.1007/s11214-017-0409-x

N. Murdoch, D. Mimoun, R.F. Garcia, W. Rapin, T. Kawamura, P. Lognonné, D. Banfield, W.B. Banerdt, Evaluating the wind-induced mechanical noise on the InSight seismometers. Space Sci. Rev. **211**, 429–455 (2017a). https://doi.org/10.1007/s11214-016-0311-y

N. Murdoch, B. Kenda, T. Kawamura, A. Spiga, P. Lognonné, D. Mimoun, W.B. Banerdt, Estimations of the seismic pressure noise on Mars determined from Large Eddy Simulations and demonstration of pressure decorrelation techniques for the InSight mission. Space Sci. Rev. **211**(1–4), 457–483 (2017b). https://doi.org/10.1007/s11214-017-0343-y. arXiv:1704.05664

Y. Nishikawa, A. Araya, K. Kurita, N. Kobayashi, T. Kawamura, Designing a torque-less wind shield for broadband observation of marsquakes. Planet. Space Sci. **104**, 288–294 (2014). https://doi.org/10.1016/j.pss.2014.10.011

M.P. Panning, P. Lognonné, W.B. Banerdt, R. Garcia, M. Golombek, S. Kedar, B. Knapmeyer-Endrun, A. Mocquet, N.A. Teanby, J. Tromp, R. Weber, E. Beucler, J.F. Blanchette-Guertin, E. Bozdağ, M. Drilleau, T. Gudkova, S. Hempel, A. Khan, V. Lekić, N. Murdoch, A.C. Plesa, A. Rivoldini, N. Schmerr, Y. Ruan, O. Verhoeven, C. Gao, U. Christensen, J. Clinton, V. Dehant, D. Giardini, D. Mimoun, W.T. Pike, S. Smrekar, M. Wieczorek, M. Knapmeyer, J. Wookey, Planned products of the Mars structure service for the InSight mission to Mars. Space Sci. Rev. **211**(1–4), 611–650 (2016). https://doi.org/10.1007/s11214-016-0317-5

M. Pätzold, T.P. Andert, G.L. Tyler, S.W. Asmar, B. Häusler, S. Tellmann, Phobos mass determination from the very close flyby of Mars Express in 2010. Icarus **229**, 92–98 (2014). https://doi.org/10.1016/j.icarus.2013.10.021

G.L. Pavlis, F.L. Vernon, Calibration of seismometers using ground noise. Bull. Seismol. Soc. Am. **84**(4), 1243–1255 (1994)

L. Pou, D. Mimoun, R.F. Garcia, P. Lognonné, W.B. Banerdt, O. Karatekin, V. Dehant, P. Zhu, Mars deep internal structure determination using Phobos tide measurement strategy with the SEIS/InSight experiment, in *EGU General Assembly Conference Abstracts*, vol. 18 (2016), EPSC2016-8724

A. Rivoldini, T. Van Hoolst, O. Verhoeven, A. Mocquet, V. Dehant, Geodesy constraints on the interior structure and composition of Mars. Icarus **213**(2), 451 (2011). https://doi.org/10.1016/j.icarus.2011.03.024

P. Rosenblatt, V. Lainey, S. Le Maistre, J.C. Marty, V. Dehant, M. Pätzold, T. Van Hoolst, B. Häusler, Accurate Mars Express orbits to improve the determination of the mass and ephemeris of the Martian moons. Planet. Space Sci. **56**(7), 1043–1053 (2008). https://doi.org/10.1016/j.pss.2008.02.004

J.T. Schofield, J.R. Barnes, D. Crisp, R.M. Haberle, S. Larsen, J.A. Magalhães, J.R. Murphy, A. Seiff, G. Wilson, The Mars Pathfinder Atmospheric Structure Investigation/Meteorology (ASI/MET) experiment. Science **278**(5344), 1752–1758 (1997). https://doi.org/10.1126/science.278.5344.1752

B.F. Schutz, Gravitational wave astronomy. Class. Quantum Gravity **16**(12A), A131 (1999). https://doi.org/10.1088/0264-9381/16/12A/307

P.K. Seidelmann, B.A. Archinal, M.F. A'hearn, A. Conrad, G.J. Consolmagno, D. Hestroffer, J.L. Hilton, G.A. Krasinsky, G. Neumann, J. Oberst, P. Stooke, E.F. Tedesco, D.J. Tholen, P.C. Thomas, I.P. Williams, Report of the IAU/IAG Working Group on cartographic coordinates and rotational elements: 2006. Celest. Mech. Dyn. Astron. **98**(3), 155–180 (2007). https://doi.org/10.1007/s10569-007-9072-y

B. Sklar, *Digital Communications*, vol. 2 (Prentice Hall, Upper Saddle River, 2001)

F. Sohl, T. Spohn, The interior structure of Mars: implications from SNC meteorites. J. Geophys. Res., Planets **102**(E1), 1613–1635 (1997). https://doi.org/10.1029/96JE03419

G.G. Sorrells, A preliminary investigation into the relationship between long-period seismic noise and local fluctuations in the atmospheric pressure field. Geophys. J. Int. **26**(1–4), 71–82 (1971). https://doi.org/10.1111/j.1365-246X.1971.tb03383.x

A. Spiga, D. Banfield, N.A. Teanby, F. Forget, A. Lucas, B. Kenda, J.A.R. Manfredi, R. Widmer-Schnidrig, N. Murdoch, M.T. Lemmon, R.F. Garcia, L. Martire, O. Karatekin, S. Le Maistre, B. Van Hove, V. Dehant, P. Lognonné, N. Mueller, R. Lorenz, D. Mimoun, S. Rodriguez, E. Beucler, I. Daubar, M.P. Golombek, T. Bertrand, Y. Nishikawa, M. Ehouarn, L. Rolland, Q. Brissaud, T. Kawamura, A. Mocquet, R. Martin, J. Clinton, E. Stutzmann, W.M. Folkner, J. Maki, S. Tilman, S. Smrekar, W.B. Banerdt, Atmospheric science with InSight. Space Sci. Rev. **214**, 109 (2018). https://doi.org/10.1007/s11214-018-0543-0

G. Turin, An introduction to matched filters. IRE Trans. Inf. Theory **6**(3), 311–329 (1960). https://doi.org/10.1109/TIT.1960.1057571

T. Van Hoolst, V. Dehant, F. Roosbeek, P. Lognonné, Tidally induced surface displacements, external potential variations, and gravity variations on Mars. Icarus **161**(2), 281–296 (2003). https://doi.org/10.1016/S0019-1035(02)00045-3

R.J. Warburton, J.M. Goodkind, The influence of barometric-pressure variations on gravity. Geophys. J. Int. **48**(3), 281–292 (1977). https://doi.org/10.1111/j.1365-246X.1977.tb03672.x

M.A. Wieczorek, M.T. Zuber, Thickness of the Martian crust: improved constraints from geoid-to-topography ratios. J. Geophys. Res., Planets **E01**, 009 (2004). https://doi.org/10.1029/2003JE002153

E. Wielandt, Seismic sensors and their calibration, in *New Manual of Seismological Observatory Practice*, ed. by P. Bormann, E. Bergmann (Deutsches GeoForschungsZentrum, Postdam, 2013)

P.M. Woodward, in *Probability and Information Theory, with Applications to Radar*, 2nd edn., ed. by D.W. Fry, W. Higinbotham (Elsevier, Amsterdam, 1953)

C.F. Yoder, A.S. Konopliv, D.N. Yuan, E.M. Standish, W.M. Folkner, Fluid core size of Mars from detection of the solar tide. Science **300**(5617), 299–303 (2003). https://doi.org/10.1126/science.1079645

V.N. Zharkov, T.V. Gudkova, Construction of Martian interior model. Sol. Syst. Res. **39**(5), 343–373 (2005). https://doi.org/10.1007/s11208-005-0049-7

W. Zürn, R. Widmer, On noise reduction in vertical seismic records below 2 mHz using local barometric pressure. Geophys. Res. Lett. **22**(24), 3537–3540 (1995). https://doi.org/10.1029/95GL03369